Monthly Notices of the ROYAL ASTRONOMICAL SOCIETY

MNRAS **538,** 351–372 (2025) https://doi.org/10.1093/mnras/staf290
Advance Access publication 2025 February 18

Multiwavelength analysis of AT 2023sva: a luminous orphan afterglow with evidence for a structured jet

Gokul P. Srinivasaragavan [1,2,3]★ Daniel A. Perley [4] Anna Y. Q. Ho,[5] Brendan O'Connor,[6]† Antonio de Ugarte Postigo,[7,8] Nikhil Sarin [9,10] S. Bradley Cenko,[2,3] Jesper Sollerman [11] Lauren Rhodes [12,13] David A. Green [14] Dmitry S. Svinkin,[15] Varun Bhalerao,[16] Gaurav Waratkar,[16] A. J. Nayana,[17] Poonam Chandra [17,18] M. Coleman Miller,[1,2] Daniele B. Malesani [19,20,21] Geoffrey Ryan [22] Suryansh Srijan,[23] Eric C. Bellm,[24] Eric Burns,[25] David J. Titterington,[14] Maria B. Stone [26] Josiah Purdum,[27] Tomás Ahumada,[28] G. C. Anupama [29] Sudhanshu Barway [29] Michael W. Coughlin [30] Andrew Drake,[28] Rob Fender,[31] José F. Agüí Fernández,[32] Dmitry D. Frederiks,[15] Stefan Geier,[33,34] Matthew J. Graham [28] Mansi M. Kasliwal [28] S. R. Kulkarni,[28] Harsh Kumar [35] Maggie L. Li,[28] Russ R. Laher,[36] Alexandra L. Lysenko,[15] Gopal Parwani [16] Richard A. Perley,[37] Anna V. Ridnaia [15] Anirudh Salgundi [16] Roger Smith,[36] Niharika Sravan,[38] Vishwajeet Swain,[16] Christina C. Thöne,[39] Anastasia E. Tsvetkova,[15,40] Mikhail V. Ulanov,[15] Jada Vail,[5] Jacob L. Wise[4] and Avery Wold[36]

Affiliations are listed at the end of the paper

Accepted 2025 February 6. Received 2025 February 5; in original form 2025 January 5

ABSTRACT

We present multiwavelength analysis of ZTF23abelseb (AT 2023sva), an optically discovered fast-fading ($\Delta m_r = 2.2$ mag in $\Delta t = 0.74$ d), luminous ($M_r \sim -30.0$ mag), and red ($g - r = 0.50$ mag) transient at $z = 2.28$ with accompanying luminous radio emission. AT 2023sva does not possess a γ-ray burst (GRB) counterpart to an isotropic equivalent energy limit of $E_{\gamma,\,\mathrm{iso}} < 1.6 \times 10^{52}$ erg, determined through searching γ-ray satellite archives between the last non-detection and first detection, making it the sixth example of an optically discovered afterglow with a redshift measurement and no detected GRB counterpart. We analyse AT 2023sva's optical, radio, and X-ray observations to characterize the source. From radio analyses, we find the clear presence of strong interstellar scintillation (ISS) 72 d after the initial explosion, allowing us to place constraints on the source's angular size and bulk Lorentz factor. When comparing the source sizes derived from ISS of orphan events to those of the classical GRB population, we find orphan events have statistically smaller source sizes. We also utilize Bayesian techniques to model the multiwavelength afterglow. Within this framework, we find evidence that AT 2023sva possesses a shallow power-law structured jet viewed slightly off-axis ($\theta_\mathrm{v} = 0.07 \pm 0.02$) just outside of the jet's core opening angle ($\theta_\mathrm{c} = 0.06 \pm 0.02$). We determine this is likely the reason for the lack of a detected GRB counterpart, but also investigate other scenarios. AT 2023sva's evidence for possessing a structured jet stresses the importance of broadening orphan afterglow search strategies to a diverse range of GRB jet angular energy profiles, to maximize the return of future optical surveys.

Key words: relativistic processes – *(transients:)* gamma-ray bursts.

1 INTRODUCTION

A small subset of stripped-envelope core-collapse supernova explosions are accompanied by long gamma-ray bursts (LGRBs; duration $T_{90} > 2$ s; Cano et al. 2017). LGRBs are powered by accretion on to a black hole remnant or the rotational spin-down of a neutron star remnant, generating collimated ($\theta_0 \approx 10^\circ$) ultra-relativistic ($\Gamma > 100$) jets (MacFadyen & Woosley 1999). Traditionally, emission from GRBs is divided into two phases – the prompt emission in γ-rays originates from within the jets and the afterglow emission across the electromagnetic spectrum originates from the interaction of these jets with the surrounding medium (Panaitescu & Kumar 2000; van Paradijs, Kouveliotou & Wijers 2000).

There have been hundreds of optical afterglows detected through follow-up observations of well-localized LGRB triggers, along with over 50 of their associated supernovae (see, e.g. Galama et al. 1998; Hjorth et al. 2003; Hjorth 2013; Cano et al. 2017; Melandri et al. 2019a; Hu et al. 2021; Rossi et al. 2022; Kumar et al. 2022a;

★ E-mail: gsriniv2@umd.edu
† McWilliams Fellow.

Srinivasaragavan et al. 2023; Blanchard et al. 2024; Finneran, Cotter & Martin-Carrillo 2024; Srinivasaragavan et al. 2024). The advent of state-of-the art time domain surveys including the Zwicky Transient Facility (ZTF; Bellm et al. 2019; Graham et al. 2019; Masci et al. 2019; Dekany et al. 2020) have also enabled the serendipitous discovery of optical afterglows without an associated GRB trigger. Searches of GRB archives post-facto to several optical afterglow discoveries have shown a number of events possess associated GRBs not discovered by high-energy satellites (Cenko et al. 2015; Bhalerao et al. 2017; Stalder et al. 2017; Melandri et al. 2019b; Ho et al. 2022). Possible explanations for these optical discoveries include GRBs producing γ-ray emission that do not notify GRB satellites to send out prompt alerts, or the lack of a robust afterglow localization.

If post-facto searches through GRB archives do not find observed associated γ-ray emission, these afterglows are known as 'orphan' afterglows.[1] These orphan afterglows may arise from a few different scenarios. The simplest explanation is that GRB satellites may have missed the prompt γ-ray emission due to limited coverage in certain regions of the sky, or being turned off due to operational reasons. Another explanation is due to extremely off-axis classical GRBs. Since GRBs are ultra-relativistic, emission from the jet at early times is only observable within a viewing angle of $\theta \sim 1/\Gamma$. As the jet slows down, the relativistic beaming cone widens (Rhoads 1997; Mészáros, Rees & Wijers 1998) and by the time the afterglow generates emission at optical wavelengths, the cone could include Earth's line of sight. The invocation of a 'structured' jet is also a possible explanation, where a GRB's energy profile varies with respect to viewing angle (Granot & Ramirez-Ruiz 2010; Gottlieb, Nakar & Bromberg 2021; Gottlieb et al. 2022). For a structured jet, even slightly off-axis observers viewing an event within the jet's viewing angle but outside the jet's narrow high-Γ core would see an orphan afterglow (Nakar & Piran 2003; Rossi, Perna & Daigne 2008; Cenko et al. 2013; Salafia et al. 2015; Lamb & Kobayashi 2017; Lamb, Tanaka & Kobayashi 2018; Huang et al. 2020; Sarin et al. 2021; O'Connor et al. 2023; Freeburn et al. 2024), sometimes dubbed an 'on-axis' orphan (Nakar & Piran 2003).

Another possibility is that a GRB's jet is extremely baryon-loaded, reducing its Lorentz factor. The higher density of baryons can result in pair production processes absorbing γ-ray prompt emission, reradiating it at longer wavelengths. These baryon-loaded LGRBs have been proposed as 'dirty fireballs' (Dermer, Chiang & Böttcher 1999), though there have been no observationally confirmed dirty fireballs discovered thus far in the literature. The discovery of even one genuine dirty fireball would change our picture of GRB phenomena, confirming long-held theories that baryon-loaded jets can successfully break out of their progenitor stars (Paczyński 1998; Dermer et al. 1999). Some other proposed scenarios include stalled, choked jets forming a cocoon of shocked material that produces little to no γ-rays (Gottlieb, Nakar & Piran 2018), with the interaction of the cocoon with the surrounding medium producing an afterglow similar to classical GRB jets at a lower luminosity (Nakar & Piran 2017), and low radiative efficiency bursts (Sarin et al. 2022).

The study of optically-discovered afterglows started only around 14 yr ago. The first ever discovery was in 2011, PTF11agg (Cenko et al. 2013). The event did not have a confirmed redshift, though it was argued to be between $z = 1$ and $z = 2$. Follow-up observations using the Jansky Very Large Array (VLA; Perley et al. 2011) showed that there was a long-lived scintillating radio counterpart to the optical transient. Two other optically discovered afterglows (iPTF14yb and ATLAS17aeu) were discovered in a similar manner to PTF11agg at extragalactic distances (Cenko et al. 2015; Bhalerao et al. 2017; Stalder et al. 2017; Melandri et al. 2019b). However, searches through GRB archives after their discoveries showed that both events had associated observed γ-ray emission that high-energy satellites did not promptly send out notifications for regarding their discovery.

The discovery space for these events changed dramatically with ZTF, as its rapid near-nightly cadence and wide field of view (FOV) made it a prime instrument for discovering optical afterglows serendipitously. Through dedicated afterglow searches, 11 ZTF-discovered afterglows have been published since ZTF's inception in March 2018 (Ho et al. 2020, 2022; Andreoni et al. 2021, 2022; Li et al. 2024; Perley et al. 2025). Nine of these events have confirmed redshift measurements through optical spectroscopy and five have no associated GRB found post-facto, making them orphan events (AT 2019pim, AT 2020blt, AT 2021any, AT 2021lfa, and AT 2023lcr).

Because there have been so few orphan afterglow discoveries, studies probing the physical origins of newly discovered events are important for understanding their nature. Though optical observations are utilized for their discovery, understanding their full physical picture necessitates follow-up observations in the X-ray and radio wavelengths, where jet physics and ejecta characteristics can be probed. Indeed, modelling of AT 2021any's X-ray through radio emission suggests a possible low-Lorentz factor origin (Xu, Huang & Geng 2023) or a classical GRB missed by high-energy satellites (Gupta et al. 2022; Li et al. 2024), AT 2020blt and AT 2023lcr were best modelled as classical GRBs missed by high-energy satellites (Ho et al. 2020; Li et al. 2024), and AT 2019pim and AT 2021lfa were best modelled as originating from either low-Lorentz factor GRBs or slightly off-axis structured jet GRBs (Lipunov et al. 2022; Li et al. 2024; Perley et al. 2025).

In this work, we present the optical, radio, and X-ray observations of an orphan afterglow, ZTF23abelseb (AT 2023sva) at $z = 2.28$, making it the sixth such event presented in the literature. We utilize AT 2023sva's multiwavelength observations to physically characterize the source. The paper is organized as follows: in Section 2, we present optical, X-ray, and radio observations of AT 2023sva; in Section 3, we analyse the multiwavelength data set; in Section 4, we provide a physical interpretation of the afterglow; and in Section 5, we summarize our results and present conclusions. We note that throughout this paper we utilize a flat ΛCDM cosmology with $\Omega_m = 0.315$ and $H_0 = 67.4\,\mathrm{km\,s^{-1}\,Mpc^{-1}}$ (Planck Collaboration VI 2020) to convert the redshift to a luminosity distance and correct for the Milky Way extinction of $E(B-V)_{\rm MW} = 0.24$ (Schlafly & Finkbeiner 2011), and host galaxy extinction of $E(B-V)_{\rm host} = 0.09$ mag (see Section 3.2). All magnitudes reported in the text and figures are in the AB system.

2 OBSERVATIONS

2.1 ZTF discovery

AT2023sva was discovered by ZTF (Vail et al. 2023) at $r = 17.71 \pm 0.05$ mag, on 2023-09-17 09:38:31.20 (all times are given in UTC), at a location α (J2000) $= 00^{\rm h}56^{\rm m}59\overset{\rm s}{.}20^{\rm s}$, δ (J2000) $= +80^\circ08'44\overset{''}{.}13$. ZTF is a survey on the 48-inch telescope at Palomar Observatory that covers around 10 000 deg^2 every night (Bellm et al. 2019), enabling

[1]The term 'apparently' orphan is a more precise term to describe these events, as this is a purely observational definition. Physically, an associated GRB to some isotropic energy limit usually cannot be ruled out for optically-discovered afterglows, and it is possible that γ-ray emission may be present in these systems, but was just not observed. For brevity, we refer to these events purely as 'orphan' for the rest of the text.

it to survey the entire northern sky in the g and r bands every two nights, along with i band for certain pre-selected fields. The survey's observing system is described in Dekany et al. (2020) and transient discovery applies an image subtraction pipeline (Zackay, Ofek & Gal-Yam 2016) utilizing deep reference images of fields (Masci et al. 2019). We use the ZTF Fritz marshal to store the photometry (van der Walt, Crellin-Quick & Bloom 2019; Coughlin et al. 2023).

The line of sight MW extinction is $E(B-V)_{\rm MW} = 0.24$, corresponding to $A_V = 0.74$ mag. Correcting for MW extinction and for the host-galaxy extinction derived in Section 3.2, at a redshift of $z = 2.28$ (see Section 2.2.2), this first detection corresponds to an absolute magnitude in r band of $M_r \sim -30.0$ mag, making AT 2023sva an extremely luminous optical transient. The source was flagged by human scanners after passing a filter in the ZTF alert stream (Patterson et al. 2019) that searches for young and fast transients (described in Ho et al. 2020). The source was not detected to a limiting magnitude of $r > 20.36$ mag two nights before on 2023-09-15 05:50:11.95, implying a rapid rise rate of >1.3 mag day^{-1}. There was no host galaxy counterpart detected in the ZTF reference images (the deepest upper limit was $g > 20.7$ mag) nor in Pan-STARRS images of the field. The source also decayed rapidly, at a rate of 3 mag day^{-1} in the r band after the initial observations.

Optically discovered afterglows are classified and differentiated from false positives by their rapid rises and decays, red colours indicative of a synchrotron spectrum, extragalactic redshifts, and extremely high luminosities (a full description of how optical afterglows are discovered in ZTF's alert stream is presented in Ho et al. 2020). The primary false positives in optically-discovered afterglow searches are stellar flares in the Milky Way. These flares possess blackbody temperatures of around 10 000 K (Kowalski et al. 2013), and in the optical bands, their spectrum lies on the Rayleigh–Jeans tail. This corresponds to a spectrum with $f_\nu \propto \nu^2$, or an extinction-corrected blue colour of $g - r = -0.17$ mag. Afterglows, on the other hand, have characteristic red colours due to their synchrotron spectrum, with $f_\nu \propto \nu^{-\beta}$ where f_ν is the flux density and β is the spectral index, the exponential factor that relates the flux density of a source to its frequency. A g-band observation was obtained of AT 2023sva shortly after the initial r-band detection, of $g = 18.52 \pm 0.02$, on 2023-09-17 10:41:57.034. Extrapolating this g-band detection to the time of the first r-band detection assuming a simple power-law evolution (detailed in Section 3.1), the extinction corrected $g - r$ colour at the time of discovery is $\sim$0.5 mag. The fast-rise, red colours, and lack of a host galaxy counterpart made AT 2023sva an optically discovered afterglow candidate and motivated follow-up observations.

2.2 Follow-up observations

2.2.1 *Optical photometry*

We triggered a Target of Opportunity (ToO) programme on the Spectral Energy Distribution Machine (SEDM; Blagorodnova et al. 2018; Rigault et al. 2019) on the automated 60-inch telescope at Palomar Observatory, to obtain imaging of AT 2023sva in the g, r, and i bands. The images were processed utilizing a PYTHON-based version of the FPIPE (Fremling et al. 2016) pipeline. The pipeline includes photometric calibrations and image subtraction utilizing reference images from The Sloan Digital Sky Survey (Abazajian et al. 2009). SEDM obtained four epochs of photometry, from 2023-09-18 03:56:16.080 to 2023-09-19 03:57:27.101. These follow-up observations showed AT 2023sva's light curve (LC) rapidly decayed by 2.2 mag in r band, in just 0.74 d (see Fig. 1).

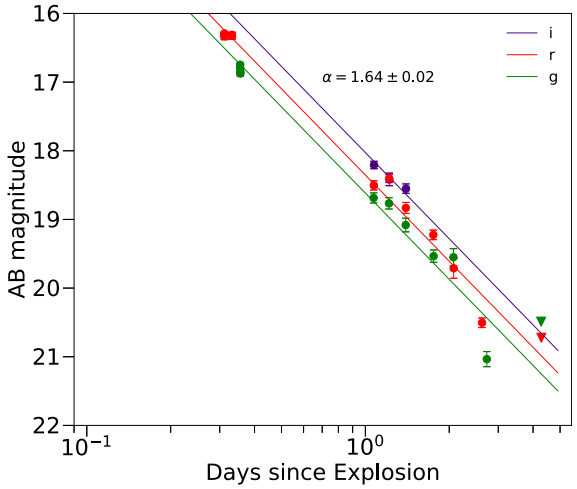

Figure 1. Optical LC of AT 2023sva in the g, r, and i bands and the earliest 3σ upper limits, along with a best-fitting power-law decay model. The photometry is taken from Table 1 and then corrected for both MW and host-galaxy extinction.

We also triggered a ToO programme on the 0.7-m GROWTH-India Telescope (GIT; Kumar et al. 2022b) located at the Indian Astronomical Observatory, Hanle-Ladakh, to obtain an additional epoch of g and r-band imaging of AT 2023sva. The observations began on 2023-09-19 17:06:25.574. We utilized the ZOGY algorithm-based PYTHON pipeline to perform image subtraction on the images using PS1 templates and to obtain the final photometry.

A single ToO observation in the g and r bands was also secured with the 2.56-m Nordic Optical Telescope (NOT), located in the Canary Islands (Spain) equipped with the ALFOSC imager, on 2023-09-18 20:15:12.96. Data reduction was carried out following standard techniques and photometric calibration was computed against the Pan-STARRS catalogue. The complete photometry obtained of AT 2023sva is presented in Table 1.

2.2.2 *Optical spectroscopy*

We secured spectroscopy of AT2023sva using OSIRIS+ (Cepa et al. 2000) on the 10.4-m Gran Telescopio Canarias (GTC) on 2023-09-19 03:55:51.011. The observation was carried out using the R1000B grism, which covers the wavelength range 3600–7800 Å, and consisted of three exposures of 900 s each (de Ugarte Postigo et al. 2023). The slit position angle was set to parallactic to minimize differential slit losses.

The data were reduced using a self-developed pipeline based on IRAF routines. Data reduction included bias and response correction and wavelength calibrations using HgAr and Ne lamps, which were also used to do a 2D distortion correction. Cosmic rays were removed using the `lacos_spec` routine (van Dokkum 2001). The 1D spectrum was obtained through optimal extraction (Horne 1986).

2.2.3 *X-ray observations*

Observations of AT 2023sva with the *Neil Gehrels Swift Observatory* (Gehrels et al. 2004) X-ray Telescope (Burrows et al. 2005) began at 2023-09-21 18:00:00.000, through a ToO trigger submitted by our team after the optical afterglow discovery. Observations lasted for 7.5 ks after the initial trigger. The data were obtained in Photon Counting mode. The transient was not detected in the observations,

Table 1. Optical photometry of AT 2023sva. The photometry in this table is not corrected for MW or host-galaxy extinction.

MJD	Filter	AB mag	Uncertainty	Facility
60204.40175	*r*	17.71	0.05	ZTF
60204.40175	*r*	17.71	0.05	ZTF
60204.40175	*r*	17.68	0.02	ZTF
60204.42189	*r*	17.71	0.05	ZTF
60204.42189	*r*	17.71	0.05	ZTF
60204.42189	*r*	17.70	0.01	ZTF
60204.44532	*g*	18.45	0.06	ZTF
60204.44532	*g*	18.39	0.02	ZTF
60204.4458	*g*	18.52	0.02	ZTF
60204.4458	*g*	18.49	0.06	ZTF
60205.16078	*g*	20.33	0.07	SEDM
60205.16243	*r*	19.89	0.07	SEDM
60205.16408	*i*	19.38	0.05	SEDM
60205.30556	*g*	20.41	0.08	SEDM
60205.30721	*r*	19.79	0.06	SEDM
60205.30887	*i*	19.59	0.09	SEDM
60205.48597	*g*	20.73	0.10	SEDM
60205.48761	*r*	20.22	0.07	SEDM
60205.48925	*i*	19.72	0.07	SEDM
60205.8439	*r*	20.61	0.07	NOT
60205.8477	*g*	21.18	0.09	NOT
60206.16083	*g*	21.20	0.12	SEDM
60206.1649	*r*	21.10	0.15	SEDM
60206.7128	*r*	21.89	0.07	GIT
60206.8192	*g*	22.68	0.11	GIT
60208.3729	*r*	>22.12	–	SEDM
60208.3666	*g*	>22.13	–	SEDM

up to a 0.3–10 keV flux limit of $< 1.2 \times 10^{-13}$ erg cm^{-2} s^{-1}. We convert this integrated flux limit to a maximum estimated flux density limit at 5 keV (to use in Section 4.1 when we model the multiwavelength data), through assuming a photon index of $\Gamma = 1.75$. We use this value, which corresponds to the optical spectral index of $\beta = 0.75$, because we determine that the X-ray and optical data likely do not lie on the same spectral segment in Section 3.2. The true X-ray spectral index must be steeper than $\beta = 0.75$, so we use $\beta = 0.75$ conservatively to extrapolate the 0.3–10 keV flux limit to the flux density limit at 5 keV, in order for the upper limit derived to be the maximum allowed. We derive a flux density upper limit at 5 keV of $< 8.65 \times 10^{-15}$ erg cm^{-2} s^{-1} keV^{-1}.

2.2.4 Radio observations

The Arcminute Microkelvin Imager–Large Array (hereafter AMI–LA) is a 8-dish interferometer based at the Mullard Radio Astronomy Observatory outside Cambridge in the UK. It observes at a central frequency of 15.5 GHz with a bandwidth of 5 GHz (Zwart et al. 2008; Hickish et al. 2018). Observations of AT 2023sva commenced with AMI–LA on 2023-09-19 02:08:35UT (1.2 d after the discovery). Each observation consisted of a series of 600 second scans of the target interleaved with 100 s of the phase calibrator J0017+8135, adding up to a total of 4 h on target (except on 2023-10-07 which was only 2 h). Once per day AMI–LA also observes a bandpass/flux calibrator 3C286. AT 2023sva was observed over 12 epochs spanning 1 to 60 d post-discovery. Data from AMI–LA is reduced using custom software REDUCE_DC (Perrott et al. 2013) which performs flux scaling, bandpass and complex gain calibration as well as flagging for radio frequency interference and antenna shadowing. The calibrated data are then output in *fits* format so they can be read into CASA for imaging and any further flagging that is required (McMullin et al. 2007). Imaging was performed interactively using *tclean* within CASA. The AMI observations are presented in Table 2.

Table 2. AMI radio observations of AT 2023sva, obtained at 15.5 GHz.

MJD	F_ν (μJy)	σ (μJy)
60206.11	220	41
60210.11	350	37
60216.01	522	106
60218.01	423	55
60221.01	455	52
60224.01	432	80
60232.91	348	33
60238.91	301	47
60240.61	392	90

We also observed AT 2023sva with the Karl G. Jansky VLA on six occasions between November 2023 and August 2024 (programme ID 24A-130). The first observation used the S, C, X, Ku, and Ka-band receivers (3, 6, 10, 15, and 33 GHz); subsequent observations used only a subset of these receivers. Data were calibrated and imaged using standard procedures in the Astronomical Image Processing System (AIPS). Flux density measurements were performed using `imfit`. The VLA observations are presented in Table 3.

We also carried out Upgraded Giant Metrewave Radio Telescope (uGMRT) observations of AT 2023sva at two epochs during March 22–31 and 2024 May 17–20. The data were recorded in standard continuum observing mode with a time integration of 10 s in bands-3 (250−500 MHz), 4 (550−850 MHz), and 5 (1000−1460 MHz). We used a bandwidth of 200 MHz in bands 3 and 4 and 400 MHz in band-5 split into 2048 channels. 3C48 was the flux density and bandpass calibrator and 2344+824 (bands-4 and 5) and 0229+777 (band-3) were the phase calibrators. We used Astronomical Image Processing Software (AIPS; Greisen 2003) to reduce the data following standard procedure (Nayana et al. 2017). The data were initially inspected for non-working antennae and radio frequency interference. The corrupted data were flagged using tasks `UVFLG`, `TVFLG`, and `SPFLG` and then calibrated. The calibrated target data were imaged using task `IMAGR` in an interactive mode followed by a few rounds of phase-only self-calibration.

2.3 Search for associated GRB

The γ-ray sky is monitored by the third Interplanetary Network (IPN), whose most sensitive instruments are the *Swift* Burst Alert Telescope (BAT), *Fermi* Gamma-ray Burst Monitor (GBM; Meegan et al. 2009), and the Konus-Wind (Barthelmy et al. 2005) instrument. We searched the archives of these three instruments, as well as the AstroSat Cadmium Zinc Telluride Imager (CZTI; Bhalerao et al. 2017) instrument, to determine if there is an associated GRB temporally and spatially coincident with AT 2023sva. We searched the time periods between the last ZTF non-detection and the first detection (see Section 2.1). Though there were several GRBs in this time period, we found no *Fermi* or *Swift* GRBs temporally and spatially coincident to AT 2023sva, through searching the *Fermi* GBM Burst Catalogue, the *Fermi* GBM Subthreshold Trigger list, and the *Swift* GRB Archive. There were reports of a candidate GRB on the Gamma-Ray Coordinates Network archives; however this counterpart was later classified as a likely solar flare and deemed unrelated to AT 2023sva (Roberts et al. 2023). Due to the 2 d time period between the last non-detection and first detection, there was

Table 3. VLA observations of AT 2023sva.

ν (GHz)	F_ν (μJy)	σ (μJy)
Epoch 1 (MJD 60276.35)		
4.53	25.2	14
5.49	49.3	13
6.43	95.6	12
7.51	108.3	11
8.49	147	14
9.51	134	13
10.48	146	14
11.49	109	18
12.5	63	20
13.5	79	14
14.5	92	14
15.6	85	15
16.6	67	16
17.6	115	18
Epoch 2 (MJD 60282.00)		
8.5	139	11
9.5	112	11
10.5	100	12
11.5	66	15
12.5	99	14
13.5	72	11
14.5	84	11
15.5	72	12
16.5	86	11
17.5	82	17
31	63.8	13.9
35	51.7	16
Epoch 3 (MJD 60287.06)		
4.5	157	13
5.5	229	12
6.5	216	11
7.5	153	10
8.5	132	12
9.5	143	12
10.5	119	13
11.5	90	16
Epoch 4 (MJD 60335.10)		
2.25	127	45
2.75	145	20
3.25	210	15
3.75	141	15
4.5	119	11
5.5	110	11
6.5	111	10
7.5	68	9
8.5	100	13
9.5	50	11
10.5	67	12
11.5	41	13
13	36	13
15	24	8
Epoch 5 (MJD 60437.90)		
2.7	40	18
3.24	110	15
3.75	136	15
4.5	64.2	9.6
5.5	39	9.4
7	21.4	6.2
9	18.4	5.1
11	17	5.5

Table 3 – *continued*

ν (GHz)	F_ν (μJy)	σ (μJy)
Epoch 6 (MJD 60537.30)		
3.5	47.5	6.6
5	35.7	6.2
7	21	5.1
9	17.3	4

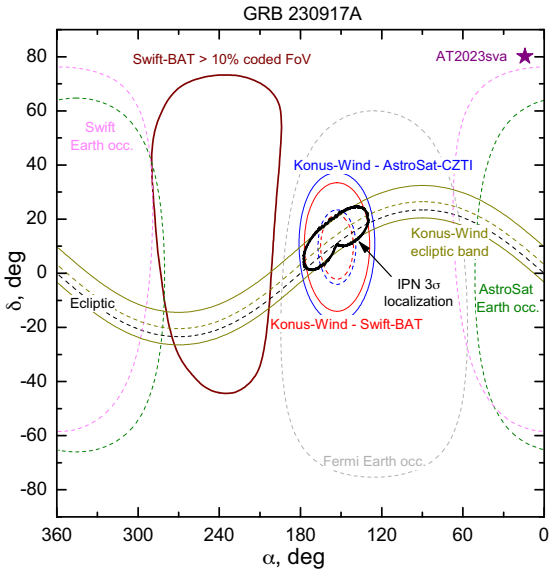

Figure 2. The IPN 3σ localization region for GRB 230917A (the thick solid black line), compared to the point-source location of AT 2023sva (star). In addition, we show the *Swift*-BAT FOV (the solid white line), the Earth occulted regions for *Swift*, *Fermi*, and Astrosat-CZTI (dashed lines), the ecliptic plane (the dashed black line), the Konus-Wind ecliptic latitude constraint (the solid dark green lines indicates the 3σ uncertainty and the dashed dark green line indicates the most probable burst source ecliptic latitude), the Konus-Wind–AstroSat-CZTI and Konus-Wind–*Swift*-BAT 3σ triangulation annuli (solid blue and red lines), and the most probable burst location utilizing the Konus-Wind–AstroSat-CZTI and Konus-Wind–*Swift*-BAT triangulation (dashed blue and red lines). We conclude that GRB 230917A is not associated with AT 2023sva.

a significant amount of time that both *Fermi* and *Swift* were not viewing the field of AT 2023sva due to being occulted by the Earth.

However, because of Konus-Wind's 4π FOV and its interplanetary orbit at the Earth–Sun L1 Lagrange point, AT 2023sva's location was always visible to the instrument. Konus-Wind detected two GRBs not detected by *Fermi* during the time period of interest. The first, which occurred on 2023-09-15 06:54:20, resulted in Konus-Wind's ecliptic latitude response clearly being inconsistent with AT 2023sva's position. Both Konus-Wind and AstroSat-CZTI detected the second GRB, GRB 230917A on 2023-09-17 00:44:38.873 by Konus-Wind and on 2023-09-17 00:44:43.5 by Astrosat-CZTI (Navaneeth et al. 2023). We utilized the propagation time delay between Konus-Wind and AstroSat-CZTI and the Konus-Wind ecliptic latitude response to calculate the 3σ IPN localization region and determine if it is consistent with the position of AT 2023sva.

We show the localization region in Fig. 2, along with contours showing various Earth-occulted regions for the different satellites, along with the $>$ 10 per cent coded FOV of *Swift*. We see that GRB 230917A's 3σ localization region is clearly not consistent

with AT 2023sva's location. The lack of detections from *Fermi* and *Swift* are also consistent with this localization, as GRB 230917A's location was occulted by the Earth for *Fermi* and was outside *Swift*'s coded FOV. We also localized the burst through the AstroSat-CZTI localization framework (Saraogi et al. 2024). Since the burst was not bright, the localization was quite coarse, placing AT 2023sva within the 57 per cent contour. This also supports the possibility that the burst may not be associated with the optical transient. Therefore, we determine that AT 2023sva does not possess a detected GRB counterpart.

We calculate the AstroSat-CZTI upper limits in the time window between the last non-detection and first detection (a window size of 21 600 s; with a confidence of 97.44 per cent), utilizing the methodology in Sharma et al. (2021). We analysed AstroSat-CZTI's duty cycle during the 50+ h window (∼19 AstroSat-CZTI orbits) between the first non-detection and detection. With the source's high declination, AstroSat had continuous visibility of the source, but ∼29 per cent of the time was lost to South Atlantic Anomaly downtime and 3 per cent to slewing. AstroSat-CZTI detects a confident GRB approximately every 120 h. Our extended time window significantly increases the false alarm rate, leading to the flux upper limits having a relatively low confidence (∼87 per cent). Additionally, the method for estimating flux limits requires 10 'witness' neighbouring orbits, which is insufficient to reliably estimate the background for our time window. As a result, the upper limits we derived were not meaningful.

We then utilize the Konus-Wind non-detection to derive a peak flux upper limit for AT 2023sva's GRB counterpart. During the interval of interest Konus-Wind was continuously observing the whole sky in the waiting mode with temporal resolution 2.944 s. In this mode count rates are recorded in the three energy bands: 19–80 keV (G1), 80–325 keV (G2), and 325–1290 keV (G3). The instrument background count rate varied slowly at time-scale of a day at < 7 per cent. There were a number of minor data gaps of a size of about a few $\times 2.944$ s, accounting for 4 per cent of the time between the last non-detection and first detection. After the trigger on GRB 230917A, there was an hour long data gap in the waiting mode record due to instrument data readout. During this interval, only the G2 count rate was available with ∼4 s resolution.

Using the waiting mode data free from GRBs detected in the time period between the last non-detection and first detection of AT 2023sva and the response for AT 2023sva's position, we estimate an upper limit (90 per cent confidence) on the 20–1500 keV peak flux to 1.5×10^{-7} erg cm^{-2} s^{-1} for a typical LGRB spectrum (a Band function with $\alpha = -1$, $\beta = -2.5$, $E_{\rm peak} = 300$ keV) and a 2.944 s time-scale. The lack of a detected GRB counterpart suggests that AT 2023sva's limiting fluence is comparable to that of the weakest burst from Tsvetkova et al. (2021), who did a study on Konus-Wind bursts simultaneously detected by *Swift*-BAT. This fluence is 4×10^{-7}erg cm^{-2} and given the redshift $z = 2.28$, this corresponds to an isotropic equivalent energy upper limit of $E_{\gamma,\rm iso} < 1.6 \times 10^{52}$ erg for AT 2023sva's GRB counterpart.

3 OPTICAL AND RADIO ANALYSIS

3.1 Optical LC

We show the optical LC in Fig. 1 and the optical transient fades very rapidly. There is a possible break in the LC that occurs between one to two days after explosion; however, this break cannot be constrained because of the transient's rapidly fading nature. This leads to a lack of detections at later times to truly constrain the presence of a break (or lack thereof). Therefore, we fit a simple power law to the early-time data in g, r, and i bands simultaneously with different normalization factors, $F_\nu \propto (t - t_0)^{-\alpha}$, where α is the power-law decay index, and t_0 is the estimated time of explosion. We set t_0 equal to the best-fitting time of explosion derived in Section 4.1, of $t_0 = 60204.09$ MJD, or 7.5 h prior to the first detection. We refer to this t_0 as the time of explosion for the rest of this work. We note that we did try to let t_0 be a free parameter in the fit as well. Through this fitting procedure, we found that t_0 was constrained to the midpoint between the last non-detection and the first detection, likely due to the small number of data points. Before fitting a power law, we first correct the optical magnitudes for both the Milky Way ($E(\rm B-V)_{\rm MW} = 0.24$ mag), and host galaxy ($E(B-V)_{\rm host} = 0.09$; see Section 3.2) extinction. We derive a power-law decay index $\alpha = 1.64 \pm 0.02$.

From our best-fitting LC, we see that the single power-law decay model does not fit the last epoch of observations well. This is due to the possible break in the LC mentioned earlier, which is likely from the synchrotron cooling frequency $\nu_{\rm c}$ passing through the optical bands, resulting in a change of the temporal power-law decay index of the LC (Granot & Sari 2002; Ryan et al. 2020). We provide more evidence for this in Section 4.1.

3.2 Optical SED and spectroscopy

We fit the gri data from SEDM taken over three separate epochs (detailed in Table 1) to a spectral power-law model $F_\nu \propto \nu^{-\beta}$, after correcting for the Milky Way extinction. We obtain a spectral index of $\beta = 0.95 \pm 0.15$. When including the X-ray upper-limit in the fitting extrapolated to the midpoint of the SEDM observations, we constrain the optical to X-ray spectral index $\beta_{\rm OX} > 1.1$. Therefore, we determine that the X-ray and optical data likely do not lie on the same spectral segment.

In Fig. 3, we show the OSIRIS spectrum of AT 2023sva (details of observations in Section 2.2.2). The spectrum shows a clear Lyman-α feature and various other absorption features, at a redshift $z = 2.280 \pm 0.002$. We measure the equivalent widths of the O I, C IV, and Fe II absorption features. We find strengths of 1.9 ± 1.1, 2.63 ± 0.70, and 1.42 ± 0.56 Å. We then compare the line strengths of AT 2023sva with other GRBs in the literature through calculating the line strength parameter (LSP), described in de Ugarte Postigo et al. (2012). We calculate a LSP of -1.70 ± 0.58, which corresponds to the 1.03th percentile of GRBs. Therefore, 99 per cent of the GRBs in the literature have line strengths greater than AT 2023sva, pointing towards an extremely low-density sight line to the source.

Because only an X-ray upper limit was obtained, we could not make any inferences about the presence of host-galaxy extinction from the SED fitting. However, in Fig. 3, we see that the Milky Way extinction-corrected spectrum shows a distinct curvature that is likely due to extra extinction from the host galaxy. Therefore, we fit a power law to the optical spectrum with the addition of host-galaxy extinction as a free parameter, using the Cardelli, Clayton & Mathis (1989) extinction law, with $R_v = 3.1$. We find a best-fitting spectral index of $\beta = 0.75 \pm 0.07$ and $E(B-V)_{\rm host} = 0.09 \pm 0.01$ mag. We note that there is no prominent 2175 Å feature in the spectrum, which is a characteristic feature of the Cardelli et al. (1989) model. It has also been shown that GRB host galaxies in general rarely show strong evidence for this feature, though in most cases it also cannot be ruled out (Schady et al. 2012). Therefore, the uncertainties reported here are statistical uncertainties and there are likely larger uncertainties dominated by the use of a particular extinction model.

3.3 Closure relations

There are characteristic closure relations between α, β, and p (the electron spectral index) that correspond to different astrophysical

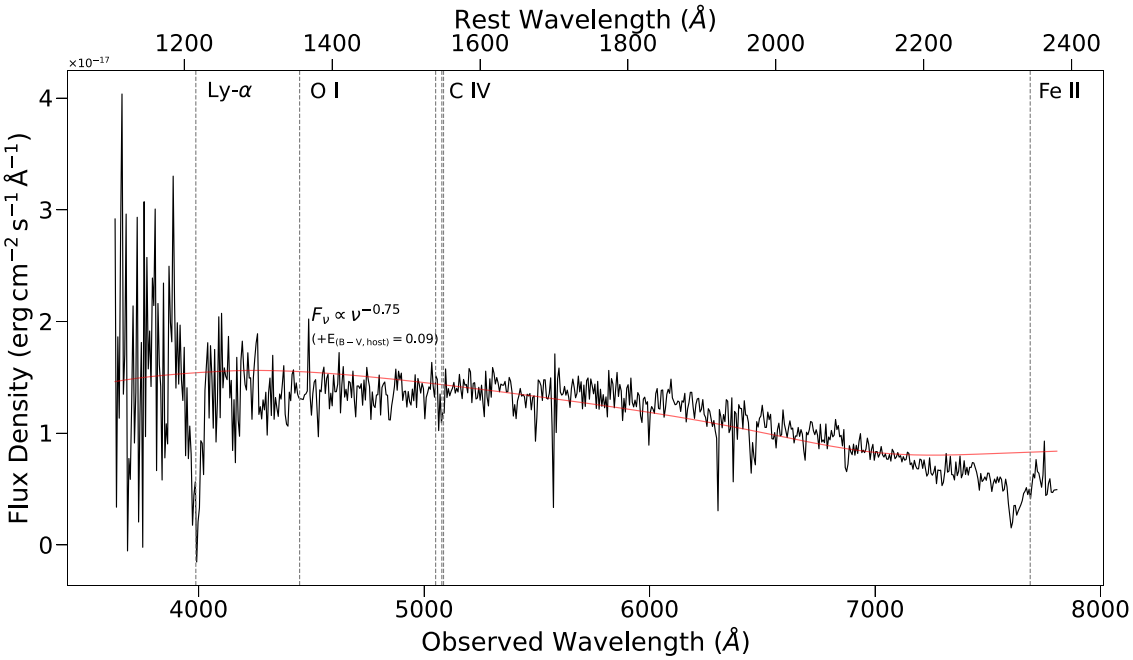

Figure 3. Optical spectrum of AT 2023sva, obtained by the OSIRIS instrument (details in Section 3.2). We show the Lyman-α absorption feature along with absorption features characteristic to GRB afterglows at a redshift $z = 2.280 \pm 0.002$, and a best-fitting spectral power-law model with additional host-galaxy extinction (details in Section 3.2).

environments (a constant density ISM environment or a stellar wind environment), as well as cooling regimes within the synchrotron spectrum (Sari, Piran & Narayan 1998; Granot & Sari 2002). We test the values derived for α and β within these regimes, assuming a standard, tophat jet structure. First, we determine whether we are in the fast or slow cooling regime. In the fast cooling regime, the synchrotron frequency corresponding to the minimum Lorentz factor that electrons are accelerated to in the shockwave in the context of a power-law distribution (ν_m, also known as the peak frequency) is larger than the synchrotron cooling frequency ν_c, so most electrons are expected to quickly cool to ν_c. In this regime, the optical bands can either be below ν_m ($\nu_c < \nu < \nu_m$) or above ν_m ($\nu_c < \nu_m < \nu$). For the case where $\nu_c < \nu < \nu_m$, $\beta = 0.5$ (Sari et al. 1998; Granot & Sari 2002) for both the ISM and wind environment. For the case where $\nu_c < \nu_m < \nu$, $\beta = p/2$ for both environments (Sari et al. 1998; Granot & Sari 2002). It is clear that the β we derive is not consistent with the $\nu_c < \nu < \nu_m$ case. Furthermore, if the optical bands were above the peak frequency, then that would imply $p = 1.5 \pm 0.14$. This is an abnormally small, non-physical value for p, which is generally expected to be between 2 and 3 (Curran et al. 2010). Therefore, this implies that we are not in a fast cooling environment.

For a slow cooling environment, ν_m is less than ν_c and electron cooling is not efficient. In this regime the optical bands can be either below or above ν_c. If $\nu_m < \nu < \nu_c$, then $\beta = (p-1)/2$, for both an ISM and wind environment. This would imply $p = 2.50 \pm 0.14$, which is a reasonable value. If $\nu_m < \nu_c < \nu$, $\beta = p/2$ for both environments, this implies $p = 1.50 \pm 0.14$, which again is an unreasonable value. So from this analysis, we determine that assuming a tophat jet, we are in a slow cooling environment where the optical bands are below the cooling frequency. For a constant density ISM environment, $\alpha = 3\beta/2$ in this regime (Sari, Piran & Halpern 1999), which would imply $\alpha = 1.13 \pm 0.15$, which clearly does not match the derived value of $\alpha = 1.64 \pm 0.02$. For the wind environment, $\alpha = (3\beta + 1)/2$ in this regime, which would imply $\alpha = 1.63 \pm 0.15$. This is consistent with our observed α. However, the jet's structure may be more complex than just a tophat and we revisit the closure relations within this context in Section 4.1.

3.4 Radio LC and SED

The radio LC at select frequencies is shown in Fig. 4. We see that the 15.5 GHz LC shows a gradual rise ($t^{0.4}$) at early times, until around ten days after the explosion. The LC then exhibits a shallow decay ($t^{-0.5}$) and thereafter transitions to a steep decay (t^{-2}), seen at lower frequencies as well. Lower frequency (<11 GHz) observations begin at around day 70 and there is significant short-term variability in the first couple of epochs in the 4 and 5 GHz LCs, likely indicative of strong interstellar scintillation (ISS). The initial rise in the 15.5 GHz LC until around 10 d and then shallow decay until around 70 d, can be attributed to the spectral break ν_m passing through the 15.5 GHz band. The subsequent steepening across all frequencies is most likely attributed to a jet break. We model the radio LC in Section 4.1.

In Fig. 5, we show the coeval radio SEDs, at six different epochs presented in the observer frame. We see that the SED at 72 d has multiple sharp spectral breaks. This is due to ISS and the modulations are a factor of ∼2. We see this behaviour continues to persist at lower frequencies until the epoch at 131 d, though the strength of the scintillation diminishes.

We expect ν_m to pass through the radio bands over time, leading to spectral breaks in the SEDs. Due to the variability caused by ISS, we were not able to identify any clear breaks in the first two epochs. However, starting from the epoch at 84 d, we see that the spectrum shows a clear rise and peak at low frequencies and the location of the peak moves lower in frequency space, until it is not visible anymore in the 333 d spectrum, starting from ∼10 GHz in the 72 d epoch to ∼3 GHz in the 234 d epoch. We likely are still below the cooling frequency ν_c at the times the SEDs were taken, as we do not see a steepening of the power law at later times. We fit a spectral power-law

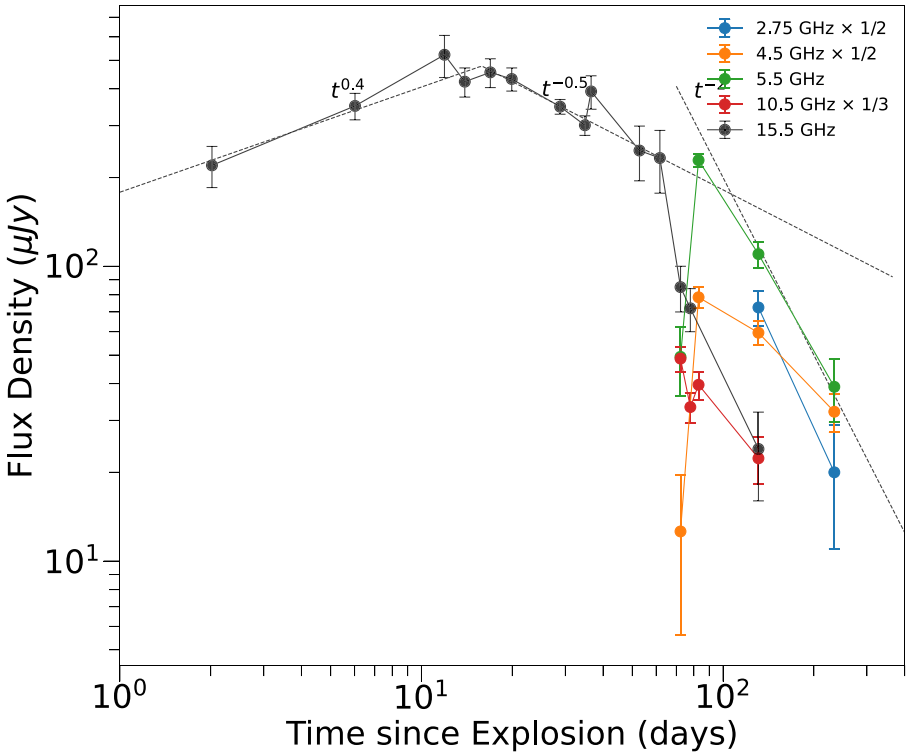

Figure 4. The AMI (15.5 GHz) and VLA (15.5 GHz and other frequencies) radio LCs with respect to the observed time since explosion. The 15.5 GHz LC is the most well-sampled over time and we fit a power law to the initial rise, shallow decay, and then the steep decay. This behaviour is most likely attributed to the peak synchrotron frequency passing through the radio bands and then a jet break at late times. The lower frequency radio LCs show high variability, due to the presence of ISS.

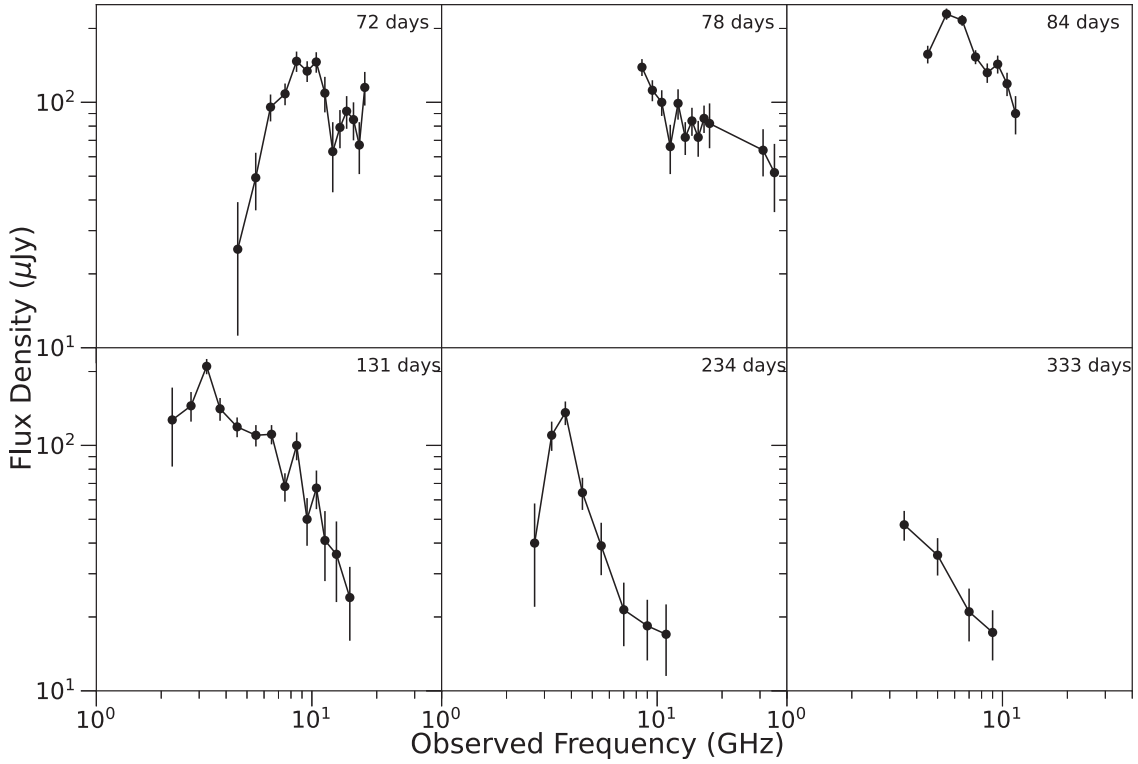

Figure 5. VLA Radio SEDs of AT 2023sva, with the observer frame time of the epochs with respect to the best-fitting explosion time shown in the plots. The spectrum at 72 d shows multiple sharp spectral breaks due to the presence of ISS. The sharp breaks continue at lower frequencies until the epoch at 131 d.

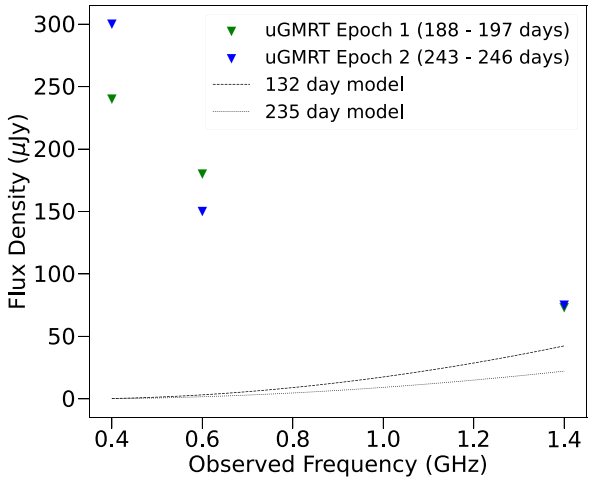

Figure 6. uGMRT observations of AT 2023sva, where the upside down markers represent the 3σ derived upper limits. Two power-law models corresponding to the low-frequency VLA observations at 131 and 234 d are also shown and the upper limits are consistent with the VLA observations.

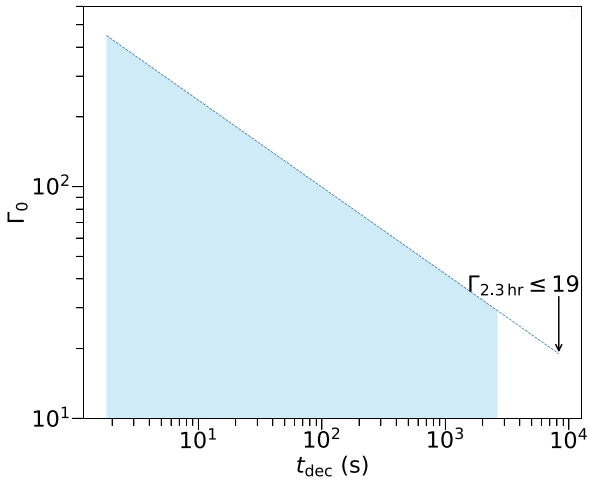

Figure 7. Upper limit on the initial Lorentz factor Γ_0 plotted against the assumed rest-frame deceleration time t_{dec}. The limit is derived from the limit obtained from scintillation analysis in Section 3.5 and assuming $\Gamma \propto t^{-3/8}$. The allowed values are shown as the shaded region.

model ($F_\nu \propto \nu^{-\beta}$) to every spectral epoch except for the 72 d epoch, both to the regions below and above ν_{m}. For frequencies below ν_{m}, we find an average value of $\beta = 2.2$, with a range of 1.4 to 4.1, and for frequencies above ν_{m}, we find an average value of $\beta = -1.2$, with a range of -0.5–-2.1. We note that the spectral indices derived below ν_{m} have large error bars and are poorly constrained, as there are only two points below the peak frequency in the 84 d epoch and three points in the 131 and 234 d epochs.

In Fig. 6, we also show the low frequency uGMRT observations. Radio emission was not detected at the source position in any of the GMRT maps providing 3-sigma flux density limits of $< 75\,\mu$Jy at 1.4 GHz, $< 180\,\mu$Jy at 0.6 GHz, and $< 300\,\mu$Jy at 0.4 GHz at the source position. The first observation took place between 188 and 197 d after t_0 and the second took place between 243 and 246 d after t_0. The upper limits derived are consistent with the power laws derived from fitting the 131 and 235 d epochs.

3.5 Constraints from radio scintillation

The radio SED shows clear variations in frequency space in the earliest epoch at 72 d, across all frequencies. The radio LC also shows clear modulations by a factor of $\sim$2 at lower frequencies up to 100 d. We interpret these variations as being due to ISS, which is the result of small-scale inhomogeneities in the ISM, which change the phases of incoming wavefronts of radio sources. Because the line of sight from Earth to the source changes as the Earth moves, this causes a change in flux, due to scattering from electrons along the line of sight through our Galaxy. There is a characteristic transition frequency ν_{ss} where strong scattering transitions ($\nu < \nu_{\mathrm{ss}}$) to weak scattering ($\nu > \nu_{\mathrm{ss}}$). GRB radio observations are expected to be affected by ISS (e.g. Granot & van der Horst 2014) and analysing their ISS can provide insights towards their angular size and Lorentz factors.

We utilize a similar method that Perley et al. (2025) used for AT 2019pim, to derive AT 2023sva's source size. From figs 1–2 of Walker (1998) (erratum Walker 2001), we determine that the transition frequency ν_{ss} along the line of sight of AT 2023sva is $\sim$15 GHz and the Fresnel scale at that frequency is $\theta_{\mathrm{F0}} \approx 2\,\mu$arcsec. At the angular diameter distance of AT 2023sva, this corresponds to a physical size of 5.2×10^{16} cm. From the radio SED in Fig. 5, we see that there is strong ISS at ν_{ss} during the earliest epoch at 72 days and it significantly decreases in later epochs. For strong ISS to exist near ν_{ss}, the source size must be comparable or smaller than the physical size corresponding to the Fresnel scale. Therefore, we estimate AT 2023sva's physical size to be at most 5.2×10^{16} cm at 72 d. Converting this to an average Lorentz factor in the rest-frame, we get $\Gamma_{\mathrm{av,22.0\,d}} \leq 2.4$. In the ISM, as the jet is decelerating, the projected size increases over time as $R \propto t^{5/8}$, or $\Gamma \propto t^{-3/8}$ (Galama et al. 2003). Extrapolating the ISS limit to the time of first detection (7.5 h after explosion in the observer frame, or 2.3 h after in the rest frame), we derive a Lorentz factor upper limit of $\Gamma_{\mathrm{av,2.3\,h}} \leq 19$.

However, Γ at the time of first detection is different than the initial Lorentz factor, Γ_0, as it is dependent on the time of explosion and the initial deceleration time-scale, t_{dec}. If we assume that $t_{\mathrm{dec}} \sim 20$ s (Ghirlanda & Salvaterra 2022) from the explosion epoch (corresponding to the typical rest-frame time-scale for a GRB optical LC to peak) and also assume that the Lorentz factor is constant from the beginning of the explosion up to the beginning of deceleration (coasting phase), we derive an initial Lorentz factor limit at the start of deceleration of $\Gamma_0 < 178$. We note that this assumption has many caveats, as it has been shown that t_{dec} varies greatly for GRBs (Ghirlanda et al. 2018). Therefore, in Fig. 7 we show the parameter space for allowed Γ_0, given our scintillation limit, for a range of t_{dec} starting from the last non-detection and ending with the first detection. We see that if $t_{\mathrm{dec}} \gtrsim 94$ s, that $\Gamma \lesssim 100$, which would indicate a more moderately relativistic outflow than the known population of cosmological GRBs. However, our observations are not constraining enough to make this claim.

There have only been a handful of scintillation measurements for GRBs confirmed in the literature, as they necessitate high-cadence, multifrequency radio observations of GRBs out to late times. There have been seven classical GRBs whose source sizes were able to be constrained by the presence of strong ISS (GRB 970508, Frail, Waxman & Kulkarni 2000; GRB 030329, Berger et al. 2003; Taylor et al. 2004, 2005; Pihlström et al. 2007; GRB 070125, Chandra et al. 2008; GRB 130427A, van der Horst et al. 2014; GRB 161219B, Alexander et al. 2019; GRB 210702A, Anderson et al. 2023; and GRB 201216C, Rhodes et al. 2022), and four orphan afterglows (AT 2019pim, Perley et al. 2014; AT 2021any, AT 2021lfa, and AT 2023lcr; Li et al. 2024). We show the source size upper limits of these sources from the literature in Fig. 8, along with that of AT 2023sva,

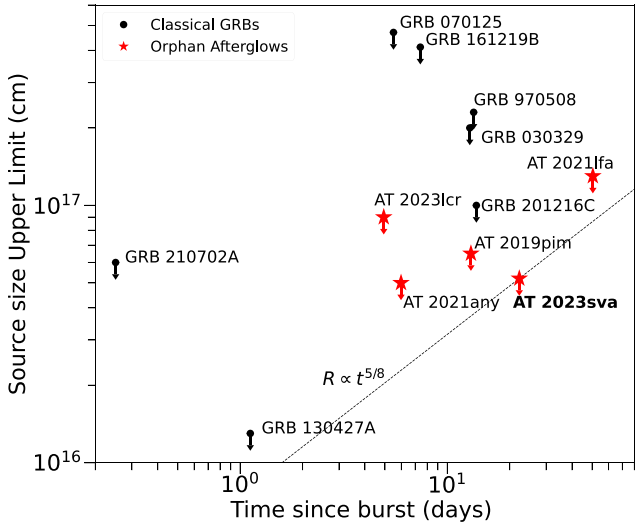

Figure 8. Comparison of source size upper limits derived from ISS analyses in seven classical GRBs (GRB 907508, GRB 030329, GRB 070125, GRB 130427A, GRB 161219B, GRB 210702A, and GRB 201216C), and five orphan afterglows (AT 2019pim, AT 2021any, AT 2021lfa, AT 2023lcr, and AT 2023sva), with respect to their rest-frame times since explosion. We also show AT 2023sva's source size upper limit as a function of time, assuming a constant density ISM environment.

along with its source size upper limit as a function of time, assuming a constant density ISM environment. We see that AT 2023sva has the smallest source size upper limit when compared to the entire population.

The source most similar to AT 2023sva in this parameter space is AT 2019pim, which possesses a source size $< 6.5 \times 10^{16}$ cm 30 d after explosion, which corresponds to ∼13 d in the rest-frame. Fig. 8 suggests that the orphan afterglow population as a whole seems to have smaller source sizes than those of classical GRB afterglows for measurements taken around the same time, as they seem to mark out a different parameter space in the plot. We note that though GRB 210702A and GRB 130427A have smaller source sizes than the rest of the population, this is mainly due to their early-time observations. When extrapolating their source sizes to around the epoch the rest of the sample was observed (∼20 d), GRB 210702A and GRB 130427A have respective source size upper limits of 10^{18} and 7×10^{16} cm.

We then utilize the Anderson–Darling test to determine if the source limits for the classical GRB and orphan afterglow sample are drawn from different statistical distributions. We derive a test-statistic of 4.78, which is greater than the critical value at the 2.5 per cent significance level of 4.59, with a p-value of 0.004. This indicates that the source size upper limits for the sample of classical GRBs and orphan afterglows with ISS source size constraints are drawn from different statistical distributions. We note that the classical GRB population analysed here is likely a biased population, as ISS analysis is usually only performed for the brightest GRBs.

One possible explanation for this difference is orphan afterglows have lower Lorentz factor origins when compared to classical GRBs, either intrinsically or due to viewing angle effects. Modelling of AT 2020blt and AT 2023lcr showed that they were best modelled as classical GRBs missed by high-energy satellites (Ho et al. 2020; Li et al. 2024). However, Li et al. (2024) showed that the inclusion of early-time data in modelling can lead to different conclusions and neither event had early-time data to constrain the afterglow's rise. AT 2021any was also modelled well as a classical GRB (Gupta et al. 2022; Li et al. 2024), though a low-Lorentz factor solution was also proposed (Xu et al. 2023). Modelling of AT 2019pim and AT 2021lfa showed that both low-Lorentz factor solutions and off-axis structured jet solutions were viable (Li et al. 2024; Perley et al. 2025), and our analysis of AT 2023sva was not able to place any constraints on the actual nature of the initial outflow at early times, as we determined it could range from highly relativistic to moderately relativistic (see Fig. 7).

Therefore, the small observed source sizes for the orphan afterglow population may not be soley due to low-Lorentz factor jets. Some other possibilities are variations in the circumstellar density within the time-scale of the observations, small-scale structure contaminating the afterglow images at later times, or stronger scintillation effects than the simple models used for this analysis (Alexander et al. 2019). Further observations of ISS in both orphan afterglows and classical GRBs are needed in order to understand if the trend holds true for a broader population, and to what extent low-Lorentz factor jets play a role.

4 PHYSICAL INTERPRETATION OF THE OUTFLOW

4.1 Multiwavelength modelling

We model AT 2023sva's LC, utilizing the open-source electromagnetic transient Bayesian fitting software REDBACK (Sarin et al. 2024), to fit different jet models from `afterglowpy` (Ryan et al. 2020). For the fitting, we utilize the *gri* optical data, the X-ray upper limit, as well as the 15.5 GHz radio LC. We do not include the lower frequency radio LCs in our fitting procedure as these frequencies are all below ν_{ss} and are affected strongly by ISS. In order to derive posteriors and perform the sampling, we utilize `bilby` (Ashton et al. 2019) and `Dynesty` (Speagle 2020).

We note that `afterglowpy` has limitations and address the relevant ones individually within the context of AT 2023sva. `afterglowpy` disables jet spreading effects when fixing a finite initial Lorentz factor for the explosion and assumes an infinite initial Lorentz factor when accounting for jet spreading. Because we lack early-time data (two days between the last non-detection and first detection) it is unlikely we will be able to place any constraints on the initial Lorentz factor through modelling. Furthermore, late-time data is largely independent of the initial Lorentz factor, as the jet would have already underwent significant deceleration, so we enable jet spreading effects in our fitting. The corner plots for our modelling are presnted in the Appendix in Figs 15, 16, and 17. We note that the corner plots still show the initial Lorentz factor as a fitting parameter even after enabling jet spreading effects; however, this is just a randomly selected value and has no actual impact on the fitting procedure.

`afterglowpy` does not account for synchrotron self-absorption (SSA), that is a primarily low-frequency radio phenomenon. Though there is a possibility that the early-time 15.5 GHz LC may be affected by SSA, its high frequency and lack of a prominent LC break at early times implies that SSA effects are negligible at that frequency. Finally, `afterglowpy` does not account for the possibility of a stellar wind medium environment surrounding the blast and assumes a constant density ISM environment. Though it is generally expected that a massive star progenitor should have a stellar wind medium, multiple previous works have shown that a constant density ISM environment still fits well to many LGRBs (though there are exceptions, e.g. Panaitescu & Kumar 2001) – Schulze et al. (2011) found that out of 27 *Swift* events, two-thirds are

Table 4. Table of priors for REDBACK fits. θ_w is ignored by the tophat model and β is only used by the power-law model.

Parameter	Unit	Description	Prior (uniform)
t_0	(MJD)	estimated burst time from first detection	[60202.24, 60204.40]
θ_v	(rad)	viewing angle	[0, 1.57]
$\log_{10}(E_{K,iso}/erg)$		isotropic equivalent kinetic energy of blast wave along jet axis	[44, 54]
θ_c	(rad)	half-opening angle of jet core	[0.01, 0.1]
θ_w	(rad)	wing truncation angle of a structured jet	$[1, 8] \times \theta_c$
$\log_{10}(n_0/cm^{-3})$		number density of protons in circumburst medium	[−5, 2]
p		power law index of relativistic electron energy distribution	[2, 3]
b		power law index of jet angular energy distribution	[0.5, 10]
$\log_{10}\epsilon_e$		fraction of thermal energy in relativistic electrons	[−5, 0]
$\log_{10}\epsilon_B$		fraction of thermal energy in magnetic field	[−5, 0]
ξ_N		fraction of accelerated electrons	[0, 1]

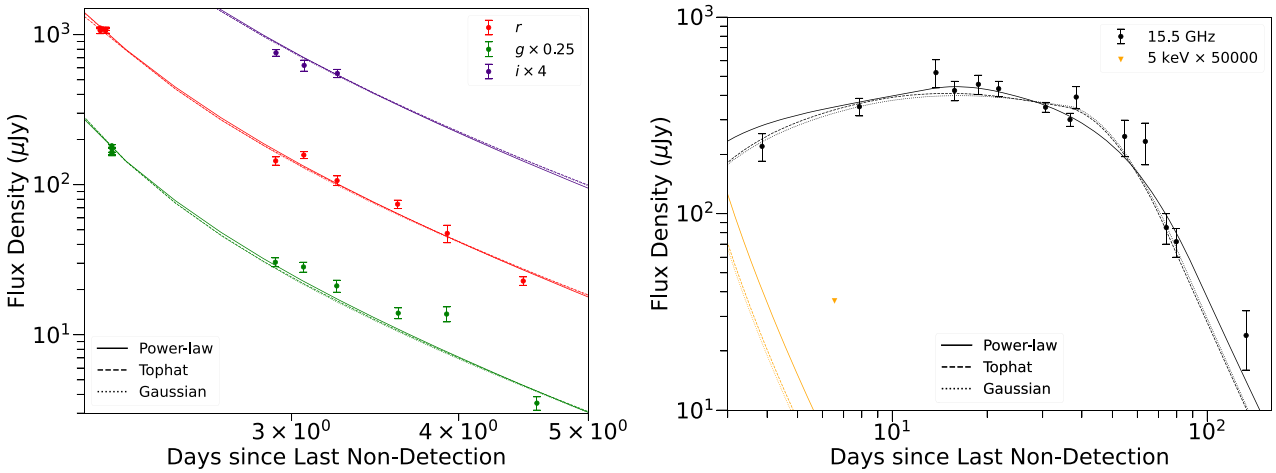

Figure 9. *Left panel*: the optical observations of AT 2023sva, along with the best-fitting power-law structured jet, tophat jet, and Gaussian structured jet fit to the observed LC. Optical fluxes have been multiplied by a constant factor for viewing purposes and have been corrected for MW and host galaxy extinction. *Right panel*: The 15.5 GHz radio observations of AT 2023sva and the X-ray upper limit, along with the best-fitting power-law structured jet, tophat jet, and Gaussian structured jet fit to the observed LC. The X-ray limit has been multiplied by a constant factor for viewing purposes.

compatible with a constant density ISM and Gompertz, Fruchter & Pe'er (2018) found that out of 56 *Fermi* events, half are compatible with a constant density ISM. Furthermore, most GRBs are modelled utilizing a constant density ISM in the literature, making it useful for future comparisons.

We test three different jet structure models from `afterglowpy` implemented in REDBACK: a tophat jet, a structured jet with a Gaussian profile, and a structured jet with a power-law profile. We show the different models fit to the optical, radio, and X-ray data in Fig. 9. Tophat jets have a constant energy per unit solid angle, where the bulk of relativistic ejecta is inside the solid angle of the jet. They can be represented by:

$$E(\theta) = \begin{cases} E_{K,\,iso},\ \theta < \theta_c \\ 0,\ \theta > \theta_c, \end{cases} \quad (1)$$

where $E(\theta)$ is the energy with respect to viewing angle, $E_{K,\,iso}$ is the isotropic kinetic energy of the jet, θ is the angle within the jet, and θ_c is the half-opening angle of the jet's core. The tophat jet has no structure and is the canonical model assumed for most GRB afterglow analyses. However, observations of some GRBs show significant evidence that their jets possess structure (more in Section 4.3), with weaker emission farther from the jet axis (e.g. Troja et al. 2019; Cunningham et al. 2020; Gill & Granot 2023; O'Connor et al. 2023). Therefore, we also test the Gaussian structured jet, which is represented by

$$E(\theta) = \begin{cases} E_{K,\,iso}(e^{-\theta^2/2\theta_c^2}),\ \theta < \theta_w \\ 0,\ \theta > \theta_w, \end{cases} \quad (2)$$

where θ_w is a 'wing truncation angle' that represents the relativistic ejecta spreading past the jet's core into wing-like structures. The third model we test is the power-law structured jet, which is represented by

$$E(\theta) = \begin{cases} E_{K,\,iso}\left(1 + \left(\frac{\theta^2}{b\theta_c^2}\right)^{-b/2}\right),\ \theta < \theta_w \\ 0,\ \theta > \theta_w, \end{cases} \quad (3)$$

where b is a power-law index that parametrizes the jet's structure.

We list the priors used for our fitting procedure in Table 4 and note that we allow for the time of explosion to also be a free parameter, due to the lack of constraints mentioned in Section 2.1. We derive the Bayesian evidences for each of the models and find $\log Z_{tophat} = 15.37$, $\log Z_{Gaussian} = 11.92$, and $\log Z_{power\ law} = 24.41$. We also calculate the Bayesian Information Criterion for every model, which accounts for possible overfitting to the data due to the use of extra parameters in the structured jet models and find $BIC_{power\ law} = -77.63$, $BIC_{Gaussian} = -68.12$, and $BIC_{Tophat} = -75.23$, where a lower BIC corresponds to a better fit. Therefore, it

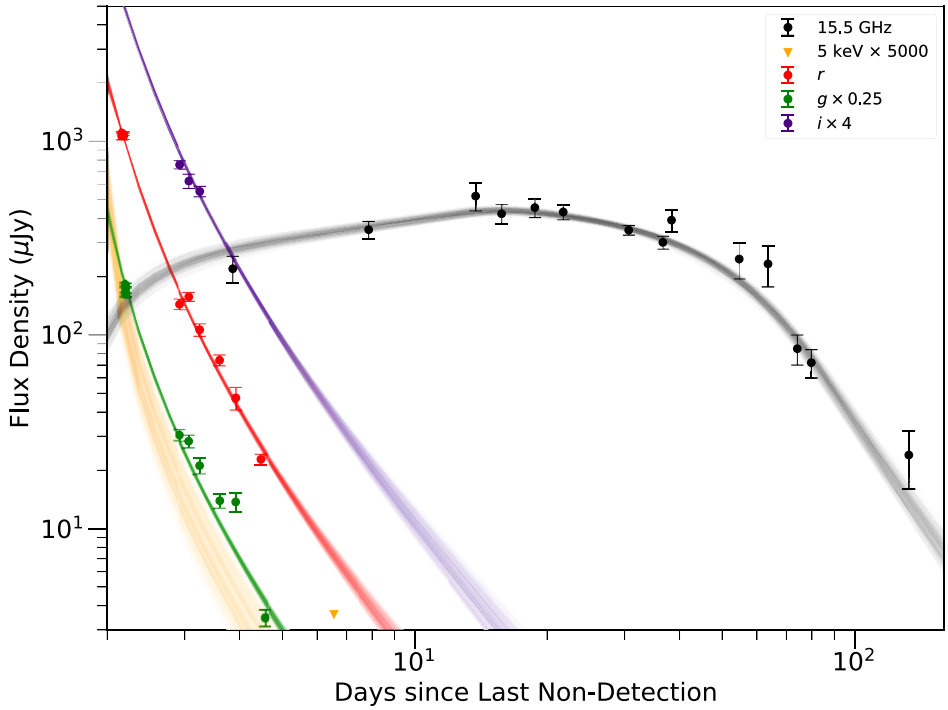

Figure 10. Multiwavelength data set of AT 2023sva, along with the 90 per cent credible interval of the predicted LCs from our posterior samples for the power-law structured jet model. Fluxes are multiplied by constant factors for visual purposes.

is clear the power-law structured jet model is favoured, within the `afterglowpy` models.

Furthermore, in both the tophat and Gaussian jet corner plots shown in the Appendix, the posterior for p is hitting the limit $p < 3$, implying that the best-fitting p is likely $p > 3$. This is not the case for the power-law structured jet–though the median p is a high value, it is constrained strongly within the priors of $p = 2.85 \pm 0.09$. From our closure relations in Section 3.3, we determined $p = 2.50 \pm 0.14$ in the regime $\nu_m < \nu < \nu_c$ – therefore, the derived p for the tophat and gaussian structured jet models is inconsistent with the p inferred from the modelling. We note that though the relations we used in that section assumed a tophat jet, the relations between β and p are identical given a structured jet (Ryan et al. 2020). This gives further evidence that a power-law structured jet is favoured.

We present the 90 per cent credible interval of the predicted LCs from the posterior samples of the power-law structured jet model, along with the full multiwavelength set of observations, in Fig. 10. We note that this is the preferred model in the context of the `afterglowpy` model and without considerations for any more complex physics contributing to the LC and spectra. Therefore, we stress that though AT 2023sva shows significant evidence for possessing a power-law structured jet within this context, we cannot definitely claim that this is the only possible scenario.

We then compute the angular size of the best-fitting power-law afterglow model's image on the sky, as a function of frequency and time, to compare it to the size derived from the ISS of the observed LC described in Section 3.5. We find that at 73 d at 15.5 GHz, the source has an angular size of $\theta \approx 1.95$ μarcsec. This is consistent with the ISS analysis (Section 3.5), where we determined that AT 2023sva's angular size needed to be comparable or smaller than the Fresnel scale (2 μarcsec). This gives us an independent confirmation that our modelling results match well with the radio observations. From the best-fitting parameters shown in Table 5, we see that we are viewing the power-law structured jet slightly off-axis, where $\theta_v \gtrsim \theta_c$. Furthermore, the power-law index of the energy distribution as a function of viewing angle is quite shallow, as we derive $b = 1.02$ for the best-fitting model and a median $\pm 1\sigma$ is $0.99^{+0.36}_{-0.24}$. We discuss the implications of this in Section 4.3.

Table 5. Final best-fitting and median $\pm 1\sigma$ parameters for the power-law structured jet model, which is the most favoured model for AT 2023sva. The best-fitting parameters correspond to the model that possesses the maximum log likelihood and the corner plot corresponding to median parameters and their 1σ confidence intervals are presented in the Appendix.

Parameter	Best-fitting result	Median $\pm 1\sigma$
t_0 (MJD)	60 204.09	$60204.09^{+0.03}_{-0.03}$
θ_v (rad)	0.08	0.07 ± 0.02
$\log_{10}(E_{K,iso}/erg)$	53.63	$53.33^{+0.27}_{-0.21}$
θ_c (rad)	0.05	0.06 ± 0.02
θ_w (rad)	$7.71 \times \theta_c$	$6.81^{+0.79}_{-1.01} \times \theta_c$
$\log_{10}(n_0/cm^{-3})$	1.41	$1.40^{+0.40}_{-0.74}$
p	2.84	2.85 ± 0.09
b	1.02	$0.99^{+0.36}_{-0.23}$
$\log_{10} \epsilon_e$	−0.77	$-0.53^{+0.18}_{-0.28}$
$\log_{10} \epsilon_B$	−3.32	$-3.18^{+0.45}_{-0.26}$
ξ_N	0.42	$0.70^{+0.19}_{-0.27}$

In Fig. 11, we show the simulated optical SEDs generated by `afterglowpy` utilizing the best-fitting power-law structured jet model, along with the optical observations of AT 2023sva. We see that generally the simulated SEDs match well with the observations across all epochs. Furthermore, we see there is a clear break in the optical SED in the 0.3 d epoch at around 4×10^{14} Hz and this break moves further down in frequency over time. This is the cooling break ν_c. This implies that the optical bands lie just above the cooling

break, which is at odds with our analysis in Section 3.3, where we determined that the optical bands should lie below the cooling break to imply a physical p. This discrepancy between the two analyses can be explained by the fact that spectral breaks are smooth over orders of magnitude. Because the optical bands have barely passed ν_c at the time the spectral index was derived (∼2 d), the slope has not fully steepened yet, leading to a fulfilment of the relation in the $\nu_m < \nu < \nu_c$ regime. Furthermore, Fig. 1 shows evidence of a possible temporal break in the early-time LC, which would correspond to ν_c fully passing through the optical bands.

Given that the best-fitting model and posteriors indicate that we are viewing the jet slightly off-axis just outside the jet's core, ($\theta_v \gtrsim \theta_c$), we utilize the closure relations provided by Ryan et al. (2020) for a structured jet for misaligned viewers, to check if the relationship between α, p, and b hold true. We test the relations in two different regimes: for $\nu_m < \nu < \nu_c$ the relation is $\alpha = (3 - 6p + 3g)/(8 + g)$ and for $\nu_m < \nu_c < \nu$, the relation is $\alpha = (1 - 6p + 2g)/(8 + g)$. The g parameter accounts for the angular structure of the jet in the relations and is given by

$$g = \frac{2b(\theta_{obs} - \theta_{eff})\theta_{eff}}{b{\theta_c}^2 + {\theta_{eff}}^2}, \quad (4)$$

where for a power-law structured jet, θ_{eff} is

$$\theta_{eff} = \theta_{obs}[1.8 + 2.1b^{-1.25} + (0.49 - 0.86b^{-1.15})\theta_{obs}/\theta_c]^{-1/2}. \quad (5)$$

Utilizing the best-fitting values from the modelling, we find $\theta_{eff} = 0.044$ and $g = 0.72$. Applying the closure relations, we find $\alpha \sim 1.4$ for $\nu_m < \nu < \nu_c$ and $\alpha \sim 1.7$ for $\nu_m < \nu_c < \nu$. In Section 3.1, we found $\alpha = 1.64 \pm 0.02$, which matches well with the $\nu_m < \nu_c < \nu$ case – and from the simulated spectra in Fig. 11, we know that the optical bands lie in this regime. This gives further evidence favouring the power-law structured jet model.

4.2 Why the lack of γ-rays?

The question arises as to why we did not detect any associated γ-ray emission for AT 2023sva, at least to an upper limit of $E_{\gamma,iso} < 1.6 \times 10^{52}$ erg. Studies suggest that for structured jets, prompt γ-ray emission may only be efficiently produced in the core of the jet (e.g. Beniamini & Nakar 2019; Beniamini et al. 2020; Gill, Granot & Kumar 2020; O'Connor et al. 2023). Since the Lorentz factor of a structured jet will also decrease with angle, this leads to an increase in the opacity due to photon-pair production processes (Gill et al. 2020). A lower Lorentz factor along the line of sight will also decrease the dissipation radius of the prompt emission, so that at large viewing angles, the photospheric radius is larger than the dissipation radius, resulting in high optical depth regions (Lamb & Kobayashi 2016; Beniamini et al. 2020). These effects are highly dependent on the angular Lorentz factor profile and the initial core Lorentz factor.

Both of these effects suppress the γ-ray emission (Gill et al. 2020) and decrease the observed γ-ray efficiency, which describes how efficiently the jet converts its energy to radiation along the line of sight. Therefore, structured jets need to be viewed extremely close to on-axis to detect their associated γ-ray prompt emission (e.g. O'Connor, Beniamini & Gill 2024), even if the viewing angle is within the wing truncation angle. Through our modelling analysis, the posteriors indicate $\theta_v = 0.07 \pm 0.02$ and $\theta_c = 0.06 \pm 0.02$. Therefore, we are likely viewing AT 2023sva slightly off-axis, making this scenario a strong possibility to explain the lack of γ-rays, depending on the steepness of the angular Lorentz factor profile and initial core Lorentz factor.

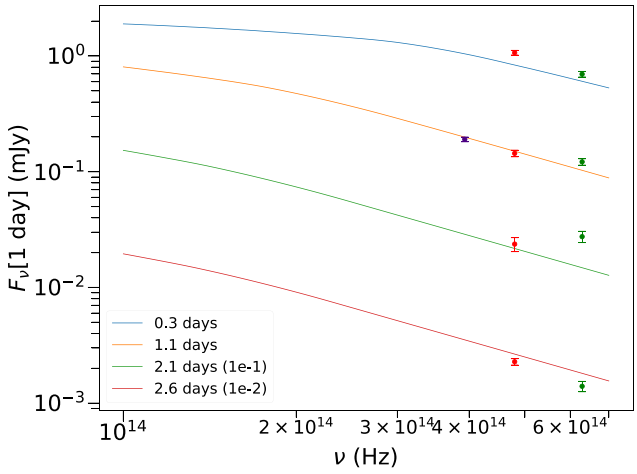

Figure 11. Simulated optical SEDs from the best-fitting power-law structured jet model and the optical observations. The fluxes are scaled for visual purposes.

We then quantify the γ-ray radiative efficiency of AT 2023sva. The radiative efficiency is calculated through

$$\eta_\gamma = \frac{E_{\gamma,iso}}{E_{K,iso} + E_{\gamma,iso}}. \quad (6)$$

Using the upper limit for $E_{\gamma,iso}$ and the 1σ range of $E_{K,iso}$ from the best-fitting power-law structured jet model, we derive $\eta_\gamma <$ 4–11 per cent. These efficiencies are on the lower end of the distribution observed from LGRBs (Wang et al. 2015), but are consistent with the ∼1 per cent efficiency derived from the internal shock model used to describe the prompt emission of bursts (Kumar 1999). Several other orphan afterglows in the literature have demonstrated possible low efficiencies–AT 2020blt (< 0.3–4.5 per cent; Sarin et al. 2022, < 0.2–17.9 per cent; Li et al. 2024), AT 2020lfa (< 0.01–0.05 per cent; Ye et al. 2024) and AT 2023lcr (< 1.3 − 3.4 per cent; Li et al. 2024), which provides evidence that the lack of associated γ-ray emission for at least some orphan afterglows may be attributed to their low radiative efficiencies.

It is important to note that these efficiencies are calculated along the line of sight, so if viewed off-axis, low efficiencies are a natural consequence of structured jets. It is also possible that on-axis jets may have intrinsic low efficiencies, as suggested for AT 2020blt in Sarin et al. (2022). It is more likely that AT 2023sva's low efficiency is due to viewing the event slightly off-axis; however, an intrinsic low efficiency cannot be ruled out, as the posteriors from the modelling do not indicate an extremely off-axis viewing angle.

If the outflow is intrinsically moderately relativistic in its core, a low Lorentz factor in comparison to classical LGRBs ($\Gamma > 100$) could be a possible reason for the lack of associated γ-rays, as pair production processes can reprocess γ-rays to X-rays if the jet is baryon-loaded, leading to a low Lorentz factor. It has been shown that even jets with moderately high Lorentz factors ($\Gamma \sim 50$) can have their high-energy emission suppressed (Lamb & Kobayashi 2016; Matsumoto, Nakar & Piran 2019). This cannot be ruled out for AT 2023sva, as its small source size at late times (see Section 3.5) gives possible evidence for this case.

Therefore, we try to measure the initial Lorentz factor Γ_0 through the relationship between Γ_0, t_{dec}, $E_{K,iso}$, and the circumburst medium density n_0, in the case of a constant density ISM environment. This

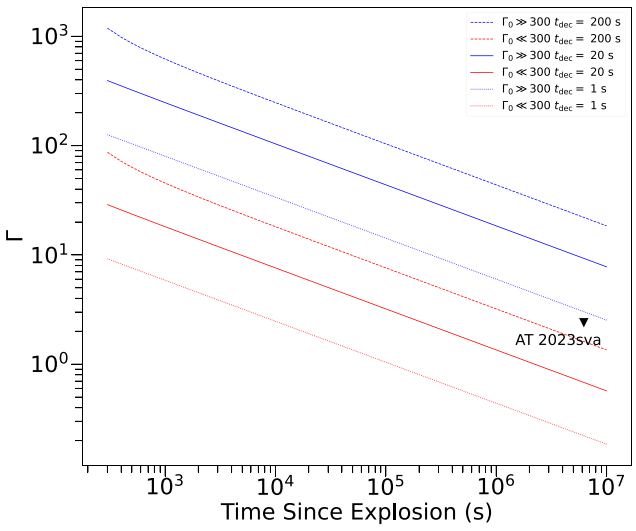

Figure 12. Comparison of the Lorentz factor evolution of $\Gamma \gg 300$ and $\Gamma \ll 300$ jet models (from Dermer et al. 1999) with respect to different observed deceleration times. We also show the upper limit for AT 2023sva's Lorentz factor at the observed time of 72 d from the scintillation analysis ($\Gamma_{\rm av,72\,d} < 2.4$).

is given by

$$\Gamma_{2.5} = \left(\frac{10\,{\rm s}(1+z)}{t_{\rm dec}}\right)^{3/8} \left(\frac{E_{53}}{n_0}\right)^{1/8}, \quad (7)$$

from Mészáros (2006), where n_0 is the number density of the circumburst medium in cm^{-3}, $E_{53} = E_{\rm K,iso}/10^{53}$ erg, and $\Gamma_{2.5} = \Gamma_0/10^{2.5}$. We first derive a lower limit, assuming that $t_{\rm dec}$ is at the time of first detection, or 7.5 h after the explosion in the observer frame (see Fig. 7 for how different assumptions of $t_{\rm dec}$ impact Γ_0). Using the full, weighted posterior distributions of $E_{\rm K,\,iso}$ and n_0 from modelling the power-law structured jet, we derive a lower limit on the initial Lorentz factor of $\Gamma_0 > 16^{+5}_{-3}$. If we assume that $t_{\rm dec}$ is 20 s in the rest frame as we did in our radio ISS analysis (see Section 3.5), we find $\Gamma_0 = 182^{+49}_{-27}$. This is consistent with the upper limit derived in Section 3.5 assuming the same $t_{\rm dec}$, where $\Gamma_0 < 178$. Again, we note that the assumed $t_{\rm dec}$ is a major caveat, as past GRBs have derived values between 1 and 1000 s (Ghirlanda et al. 2018). If $t_{\rm dec} \gtrsim 94$ s, that would imply $\Gamma_0 \lesssim 102^{+27}_{-15}$, meaning that AT 2023sva possesses ejecta more moderately relativistic than the classical GRB population. This is consistent to the limit derived in Section 3.5, where we found if $t_{\rm dec} \gtrsim 94$ seconds, that would imply $\Gamma_0 \lesssim 100$ as well.

We then test the physical models of Dermer et al. (1999) in Fig. 12. Dermer et al. (1999) introduce functions that model the synchrotron emission produced by relativistic blast waves driven from GRB jets with $\Gamma_0 \gg 300$ and $\Gamma_0 \ll 300$, that track the Lorentz factor evolution with time. Dermer et al. (1999) make the distinction between clean and dirty fireballs for these two different jets; however, true dirty fireballs are now characterized by $\Gamma \lesssim 10$. Therefore, we perform this analysis not to characterize AT 2023sva as a true dirty fireball or not, but to provide another independent constraint of the Lorentz factor. In order to do this, we utilize equations (4), (6), (11), (27), and (30) from Dermer et al. (1999), which are sensitive to n_0, $\epsilon_{\rm e}$, and ϵ_b, which we constrain to our best-fitting values from Section 4.1. These equations are also sensitive to the observed $t_{\rm dec}$ and we show a range of values for $t_{\rm dec}$ in Fig. 12, along with the Lorentz factor upper limit derived from the source size in Section 3.5.

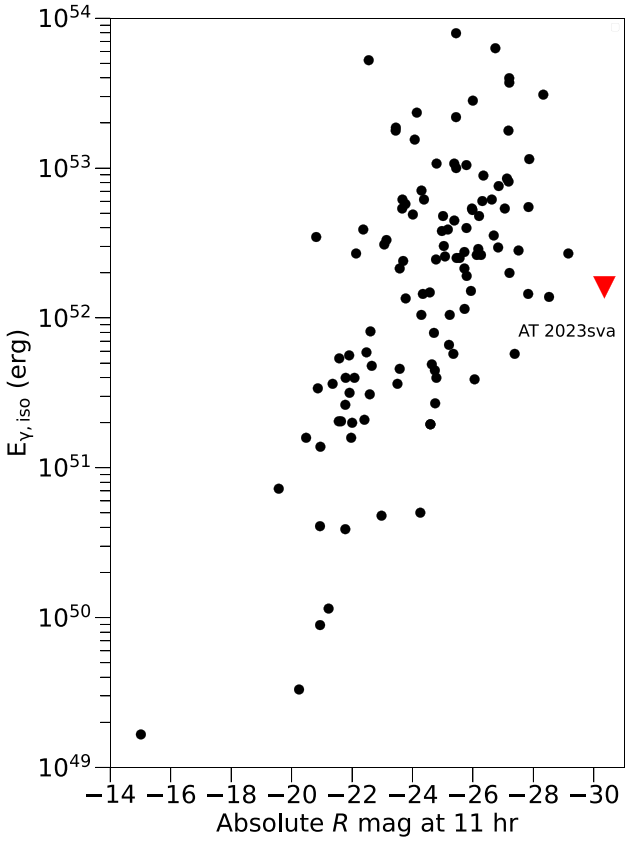

Figure 13. $E_{\gamma,\,\rm iso}$ plotted against the absolute r-band optical magnitude at 11 h for GRBs in the literature (from Nysewander et al. 2009) along with AT 2023sva, shown as a marker.

This analysis indicates that AT 2023sva originates from a jet with $\Gamma \ll 300$, which is consistent with our previous analyses. This modelling is very sensitive to the choice of n_0, $\epsilon_{\rm e}$, and ϵ_b, which is affected by the caveats associated with our afterglow modelling in Section 4.1, so it is difficult to make any more robust conclusions. Overall, through all the independent methods used to constrain Γ_0, we cannot rule out that AT 2023sva has a classical, high Γ origin, and we find that the lack of associated γ-rays is most likely due to viewing a structured jet slightly off-axis – though we also cannot rule out an on-axis, low radiative efficiency burst, or a more moderately relativistic outflow than classical GRBs. Further constraints on $t_{\rm dec}$ would allow us to place more robust constraints on Γ_0, highlighting the importance of high-cadence early-time observations in orphan afterglow observations.

4.3 Comparison to GRB afterglows

In Fig. 13, we show AT 2023sva in the context of other LGRBs in the literature (Nysewander, Fruchter & Pe'er 2009) that have measurements of $E_{\gamma,\,\rm iso}$ and an optical afterglow detection. We use the upper limit of $E_{\gamma,\,\rm iso} < 1.6 \times 10^{52}$ erg derived in Section 2.3. The optical magnitudes are all normalized to 11 h after explosion in every GRB's respective rest frame, in the rest-frame r band. Extrapolating our first observed r band measurement (corrected for galactic and host-galaxy extinction) to 11 h after explosion and utilizing $\beta = 0.75$ (see Section 3.2) to transform to the rest-frame r band, we find

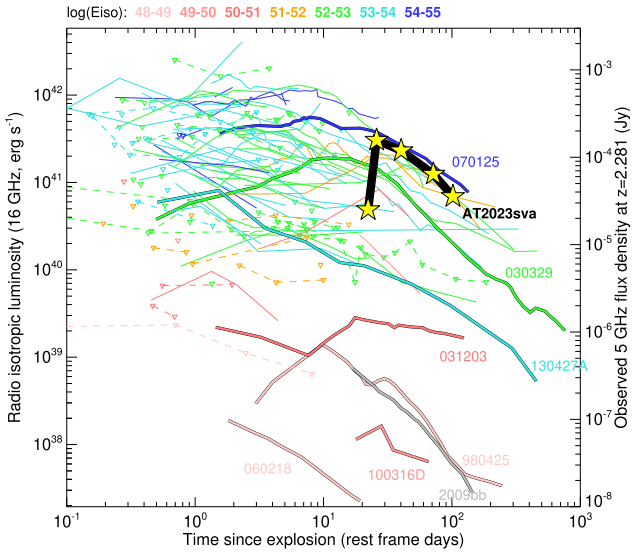

Figure 14. Comparison of AT 2023sva's radio LC (stars) to other GRB afterglow LCs from literature (Chandra & Frail 2012; Perley et al. 2014). We show the rest-frame 16 GHz luminosity LC, which corresponds to an observed flux density LC at 5 GHz at a redshift $z = 2.28$. Events are also colour-coded with respect to their $E_{\gamma,\,\mathrm{iso}}$, except for AT 2023sva.

$M_{\mathrm{abs},\,r} \sim -30.4$ mag, making it the most luminous optical afterglow in the sample.

In Fig. 14, we show AT 2023sva's radio LC compared to other GRB afterglows in the literature (plot modified from Chandra & Frail 2012; Perley et al. 2014). The LCs are plotted with respect to their 16 GHz rest-frame luminosity, which corresponds to a flux density at 5 GHz at $z = 2.28$. The flux densities were converted to luminosities through multiplying by the distance luminosity associated with $z = 2.28$. The plot is also colour-coded with respect to the GRBs' associated $E_{\gamma,\,\mathrm{iso}}$. The large rise between the first two epochs is due to ISS, as the redshift of AT 2023sva places it in a regime where the rest-frame 16 GHz LC is affected heavily by ISS. We see that AT 2023sva is quite radio-loud and most GRBs that have a similar radio luminosity have $E_{\gamma,\,\mathrm{iso}} > 10^{52}$ erg. However, in Section 2.3 we ruled out a GRB counterpart to an upper limit of $E_{\gamma,\,\mathrm{iso}} < 1.6 \times 10^{52}$ erg. This makes AT 2023sva a unique event in this parameter space.

Now, we visit AT 2023sva's preference for a structured jet model within the context of GRB afterglow jets from the literature. Structured jets have been proposed as possible models for GRB afterglows for some time, as it is natural that a jet with structure should develop due to breaking out of a dense stellar environment (e.g. Gottlieb et al. 2021, 2022). However, there have only been a few possible structured jet models inferred through afterglow analyses in the literature. GRB 030 329 showed two different jet breaks – one in the optical at around 0.55 d and another in the radio at around 9.8 d, leading to an interpretation of its afterglow as a two-component structured jet (Berger et al. 2003), though alternative models were not excluded. GRB 130427A's X-ray LC was suggested to arise from a power-law structured jet (De Pasquale et al. 2016), though other models were also discussed. GRB 160625B showed strong evidence for possessing a Gaussian-structured jet, when compared to a tophat jet or power-law structured jet (Cunningham et al. 2020). GRB 190828A was also suggested to have a two-component jet model, to discriminate between the early X-ray and optical emission and late-time X-ray and radio emission (Sato et al. 2021).

Finally, the two most famous examples of structured jets are in GRB 170817A and GRB 221009A. GRB 170817A was a short GRB that also had associated gravitational waves (e.g. Abbott et al. 2017), making it one of the most extensively followed-up astrophysical sources in history. Through extensive modelling efforts across the electromagnetic spectrum, it became clear that a structured jet was the only model that could explain the multiwavelength observations (both power-law and Gaussian structured jets are presented as viable models in various works; e.g. Lazzati et al. 2018; Margutti et al. 2018; Troja et al. 2018; Ryan et al. 2024). GRB 221009A was the brightest GRB ever detected with respect to its fluence (e.g. Frederiks et al. 2023; Lesage et al. 2023) and it is one of the most energetic GRBs ever detected (Burns et al. 2023). O'Connor et al. (2023), Gill & Granot (2023), LHAASO Collaboration (2023), and Rhodes et al. (2024) suggest that it possesses a shallow structured jet best modelled using a broken power-law energy distribution. As an alternative explanation a two-component jet model was also proposed by Sato et al. (2023).

In this work, we show evidence that AT 2023sva should be added to the above list and it is the third orphan event to show possible evidence for possessing complex jet structure. The other two are AT 2019pim (Perley et al. 2025) and AT 2021lfa (Li et al. 2024), as both of these events are modelled well by both low-Lorentz factor solutions or off-axis structured jet solutions. AT 2023sva's shallow power-law index for its structured jet's energy distribution with respect to viewing angle ($b = 0.99^{+0.36}_{-0.24}$) is similar to the index derived by O'Connor et al. (2023) for GRB 221009A, as they derived indices of 0.75 and 1.15 for their broken power-law distribution, and Gill & Granot (2023) who found an index of 0.8. However, the energetics of GRB 221009A and AT 2023sva are quite different – GRB 221009A possessed an $E_{\gamma,\mathrm{iso}} \approx 10^{55}$ erg (Lesage et al. 2023) and had strong X-ray emission. This gives evidence that the simplified jet model assumed for GRBs may need to be revised, as one of the most energetic, explosive GRBs ever detected along with an orphan event both show evidence for possessing shallow structured jets.

5 SUMMARY AND CONCLUSION

In this work, we present the discovery of an orphan afterglow, AT 2023sva, at a redshift $z = 2.28$. We analyse the optical, X-ray, and radio observations of AT 2023sva and place it in the context of GRBs in the literature. Our main findings are:

(i) AT 2023sva does not possess an associated GRB counterpart, based on a search of γ-ray satellite archives between the last non-detection and first detection of AT 2023sva (a two day window), to an isotropic equivalent energy upper limit of $E_{\gamma,\,\mathrm{iso}} < 1.6 \times 10^{52}$ erg.

(ii) There is additional host-galaxy extinction present ($E_{B-V,\,\mathrm{host}} = 0.09 \pm 0.01$), due to a characteristic curvature in the optical spectrum. Only a few absorption features are present in the spectrum and their line strengths are weaker than 99 per cent of GRBs in the literature.

(iii) The radio LC and SED shows clear presence of ISS 72 d after the explosion in the observer frame. We use this to provide an upper limit constraint on the bulk Lorentz factor in the rest frame of $\Gamma_{\mathrm{av},22.0\,\mathrm{d}} \leq 2.4$ and extrapolating back to the time of first detection, we derive a constraint of $\Gamma_{\mathrm{av},2.3\,\mathrm{h}} \leq 19$. A more stringent constraint on the initial Lorentz factor was not able to be determined, due to a lack of earlier-time observations.

(iv) AT 2023sva has a small source size upper limit (5.2×10^{16} cm) derived from ISS constraints when compared to most classical GRBs and shares scintillation properties in common with other orphan afterglows. We determine that the orphan afterglow

population has statistically lower source-size upper limits than the classical GRB population, for events whose limits were derived from ISS analyses.

(v) The model that can best reproduce the multiwavelength observations is a slightly off-axis ($\theta_v \gtrsim \theta_c$) shallow power-law structured jet, which we determined through Bayesian multiwavelength modelling of the afterglow. We only model the source in a constant density ISM and cannot rule out the possibility of the source originating from a wind medium. AT 2023sva's shallow jet structure is remarkably similar to that of GRB 221009A (Gill & Granot 2023; LHAASO Collaboration 2023; O'Connor et al. 2023; Rhodes et al. 2024).

(vi) The lack of a detected associated GRB counterpart is most likely due to viewing the structured jet slightly off-axis, just outside the opening angle of the jet's core. However, this is not the only possibility and we determine that it may be due to its lower radiative efficiency, or possibly a more moderately relativistic outflow than classical GRBs.

Because the early evolution of afterglow LCs depends strongly on the jet's structure, it is vital that orphan afterglow searches in the future calibrate their observation strategies with more complex structured jet models (e.g. Lamb & Kobayashi 2017; Lamb, Tanaka & Kobayashi 2018; Xie & MacFadyen 2019; Freeburn et al. 2024). This is incredibly important in the coming years, as new instruments like the Vera Rubin Observatory (Ivezić et al. 2019) will vastly increase the discovery space of orphan afterglows, due to increased sensitivity. However, this discovery space can only be utilized if observing strategies are broadened to incorporate the diverse range of angular energy profiles of GRB jets.

Furthermore, the recently launched Einstein Probe (EP; Yuan et al. 2022) and the Space-based multiband astronomical Variable Objects Monitor (SVOM; Wei et al. 2016) will increase the number of afterglows detected without associated γ-ray emission, through discovering their X-ray 'prompt' emission, providing another avenue for characterizing these events. In fact, EP has already began detecting GRB-related events in the soft X-rays. One such event, EP 240414a, did not have significant associated γ-ray emission (Bright et al. 2024) and was followed by the detection of an associated broad-lined Type Ic supernova (Srivastav et al. 2025; Sun et al. 2024; van Dalen et al. 2024), confirming its collapsar origin. Radio analyses constrained the outflow to have at least a moderate Γ (Bright et al. 2024), similar to AT 2023sva.

EP and SVOM are opening the door to detecting the prompt emission of events that previously would have been orphan afterglows, enabling a full characterization of their prompt and afterglow emission across the electromagnetic spectrum. Therefore, the coming years hold the tantalizing prospect of breaking historical degeneracies between different GRB models and getting closer to deciphering the landscape of relativistic jets originating from massive stellar deaths.

ACKNOWLEDGEMENTS

GPS thanks Isiah Holt for useful discussions on nested sampling techniques, Tony Piro for reading the paper on request, and Simi Bhullar for her moral support through out the paper-writing process. AYQH was supported in part by NASA grant number 80NSSC23K1155. MWC acknowledges support from the National Science Foundation with grant numbers PHY-2308862 and PHY-2117997. MBS acknowledges the Finnish Cultural Foundation grant number 00231098 and Finnish Centre for Astronomy with ESO (FINCA) grant. GCA thanks the Indian National Science Academy for support under the INSA Senior Scientist Programme. MMK acknowledges generous support from the David and Lucille Packard Foundation. BO is supported by the McWilliams Postdoctoral Fellowship at Carnegie Mellon University. AT acknowledges the financial support from 'ASI-INAF Accordo Attuativo HERMES Pathinder operazioni n. 2022-25-HH.0'.

SED Machine is based upon work supported by the National Science Foundation under grant no. 1106171. Based on observations obtained with the Samuel Oschin Telescope 48-inch and the 60-inch Telescope at the Palomar Observatory as part of the ZTF project. ZTF is supported by the National Science Foundation under grant no. AST-2034437 and a collaboration including Caltech, IPAC, the Weizmann Institute of Science, the Oskar Klein Center at Stockholm University, the University of Maryland, Deutsches Elektronen-Synchrotron and Humboldt University, the TANGO Consortium of Taiwan, the University of Wisconsin at Milwaukee, Trinity College Dublin, Lawrence Livermore National Laboratories, IN2P3, University of Warwick, Ruhr University Bochum and Northwestern University. Operations are conducted by COO, IPAC, and UW. The ZTF forced-photometry service was funded under the Heising–Simons Foundation grant #12540303 (PI: Graham). The Gordon and Betty Moore Foundation, through both the Data-Driven Investigator Programme and a dedicated grant, provided critical funding for SkyPortal.

The GROWTH India Telescope (GIT, Kumar et al. 2022) is a 70-cm telescope with a 0.7-degree FOV, set up by the Indian Institute of Astrophysics (IIA) and the Indian Institute of Technology Bombay (IITB) with funding from DST-SERB and IUSSTF. It is located at the Indian Astronomical Observatory (Hanle), operated by IIA. We acknowledge funding by the IITB alumni batch of 1994, which partially supports the operations of the telescope. Telescope technical details are available at https://sites.google.com/view/growthindia/. CZTI is built by a TIFR-led consortium of institutes across India, including VSSC, URSC, IUCAA, SAC, and PRL. The Indian Space Research Organisation funded, managed, and facilitated the project. This work is partially based on observations made with the Gran Telescopio Canarias (GTC), installed at the Spanish Observatorio del Roque de los Muchachos of the Instituto de Astrofísica de Canarias, on the island of La Palma. This work was also based on observations made with the Nordic Optical Telescope, owned in collaboration by the University of Turku and Aarhus University, and operated jointly by Aarhus University, the University of Turku and the University of Oslo, representing Denmark, Finland and Norway, the University of Iceland and Stockholm University at the Observatorio del Roque de los Muchachos, La Palma, Spain, of the Instituto de Astrofisica de Canarias. The National Radio Astronomy Observatory is a facility of the National Science Foundation operated under cooperative agreement by Associated Universities, Inc. We thank the staff of the GMRT that made these observations possible. GMRT is run by the National Centre for Radio Astrophysics of the Tata Institute of Fundamental Research. We thank the staff of the Mullard Radio Astronomy Observatory for their invaluable assistance in the operation of the Arcminute Microkelvin Imager.

DATA AVAILABILITY

All of AT 2023sva's optical photometry, radio flux densities, and X-ray upper limits are available in this article. We will make the spectrum available in the supplementary material available online.

REFERENCES

Abazajian K. N. et al., 2009, ApJS, 182, 543
Abbott B. P. et al., 2017, Phys. Rev. Lett., 119, 161101

Alexander K. D. et al., 2019, ApJ, 870, 67
Anderson G. E. et al., 2023, MNRAS, 523, 4992
Andreoni I. et al., 2021, ApJ, 918, 63
Andreoni I. et al., 2022, Nature, 612, 430
Ashton G. et al., 2019, ApJS, 241, 27
Barthelmy S. D. et al., 2005, Space Sci. Rev., 120, 143
Bellm E. C. et al., 2019, PASP, 131, 068003
Beniamini P., Nakar E., 2019, MNRAS, 482, 5430
Beniamini P., Duran R. B., Petropoulou M., Giannios D., 2020, ApJ, 895, L33
Berger E. et al., 2003, Nature, 426, 154
Bhalerao V. et al., 2017, JA&A, 38, 31
Blagorodnova N. et al., 2018, PASP, 130, 035003
Blanchard P. K. et al., 2024, Nat. Astron., 8, 774
Bright J. S. et al., 2024, preprint (arXiv:2409.19055)
Burns E. et al., 2023, ApJ, 946, L31
Burrows D. N. et al., 2005, Space Sci. Rev., 120, 165
Cano Z., Wang S.-Q., Dai Z.-G., Wu X.-F., 2017, Adv. Astron., 2017, 8929054
Cardelli J. A., Clayton G. C., Mathis J. S., 1989, ApJ, 345, 245
Cenko S. B. et al., 2013, ApJ, 769, 130
Cenko S. B. et al., 2015, ApJ, 803, L24
Cepa J. et al., 2000, in Iye M., Moorwood A. F., eds, Proc. SPIE Conf. Ser. Vol. 4008, Optical and IR Telescope Instrumentation and Detectors. SPIE, Bellingham, p. 623
Chandra P., Frail D. A., 2012, ApJ, 746, 156
Chandra P. et al., 2008, ApJ, 683, 924
Coughlin M. W. et al., 2023, ApJS, 267, 31
Cunningham V. et al., 2020, ApJ, 904, 166
Curran P. A., Evans P. A., de Pasquale M., Page M. J., van der Horst A. J., 2010, ApJ, 716, L135
de Ugarte Postigo A. et al., 2012, A&A, 548, A11
de Ugarte Postigo A., Malesani D. B., Agui Fernandez J. F., Thoene C. C., Geier S., 2023, GRB Coordinates Netw., 34740
De Pasquale M. et al., 2016, MNRAS, 462, 1111
Dekany R. et al., 2020, PASP, 132, 038001
Dermer C. D., Chiang J., Böttcher M., 1999, ApJ, 513, 656
Finneran G., Cotter L., Martin-Carrillo A., 2024, preprint (arXiv:2411.08866)
Frail D. A., Waxman E., Kulkarni S. R., 2000, ApJ, 537, 191
Frederiks D. et al., 2023, ApJ, 949, L7
Freeburn J. et al., 2024, MNRAS, 531, 4836
Fremling C. et al., 2016, A&A, 593, A68
Galama T. J. et al., 1998, Nature, 395, 670
Galama T. J., Frail D. A., Sari R., Berger E., Taylor G. B., Kulkarni S. R., 2003, ApJ, 585, 899
Gehrels N. et al., 2004, ApJ, 611, 1005
Ghirlanda G., Salvaterra R., 2022, ApJ, 932, 10
Ghirlanda G. et al., 2018, A&A, 609, A112
Gill R., Granot J., 2023, MNRAS, 524, L78
Gill R., Granot J., Kumar P., 2020, MNRAS, 491, 3343
Gompertz B. P., Fruchter A. S., Pe'er A., 2018, ApJ, 866, 162
Gottlieb O., Nakar E., Piran T., 2018, MNRAS, 473, 576
Gottlieb O., Nakar E., Bromberg O., 2021, MNRAS, 500, 3511
Gottlieb O., Liska M., Tchekhovskoy A., Bromberg O., Lalakos A., Giannios D., Mösta P., 2022, ApJ, 933, L9
Graham M. J. et al., 2019, PASP, 131, 078001
Granot J., Ramirez-Ruiz E., 2010, preprint (arXiv:1012.5101)
Granot J., Sari R., 2002, ApJ, 568, 820
Granot J., van der Horst A. J., 2014, PASA, 31, e008
Greisen E. W., 2003, in Heck A., ed., Astrophysics and Space Science Library Vol. 285, Information Handling in Astronomy – Historical Vistas. Kluwer, Dordrecht, p. 109
Gupta R. et al., 2022, JA&A, 43, 11
Hickish J. et al., 2018, MNRAS, 475, 5677
Hjorth J., 2013, Philos. T. Roy. Soc. Lond. Ser. A, 371, 20120275
Hjorth J. et al., 2003, Nature, 423, 847
Ho A. Y. Q. et al., 2020, ApJ, 905, 98
Ho A. Y. Q. et al., 2022, ApJ, 938, 85
Horne K., 1986, PASP, 98, 609
Hu Y. D. et al., 2021, A&A, 646, A50
Huang Y.-J. et al., 2020, ApJ, 897, 69
Ivezić Ž. et al., 2019, ApJ, 873, 111
Kowalski A. F., Hawley S. L., Wisniewski J. P., Osten R. A., Hilton E. J., Holtzman J. A., Schmidt S. J., Davenport J. R. A., 2013, ApJS, 207, 15
Kumar P., 1999, ApJ, 523, L113
Kumar A., Pandey S. B., Gupta R., Aryan A., Ror A. K., Sharma S., Brahme N., 2022a, New A, 97, 101889
Kumar H. et al., 2022b, AJ, 164, 90
LHAASO Collaboration, 2023, Science, 380, 1390
Lamb G. P., Kobayashi S., 2016, ApJ, 829, 112
Lamb G. P., Kobayashi S., 2017, MNRAS, 472, 4953
Lamb G. P., Tanaka M., Kobayashi S., 2018, MNRAS, 476, 4435
Lazzati D., Perna R., Morsony B. J., Lopez-Camara D., Cantiello M., Ciolfi R., Giacomazzo B., Workman J. C., 2018, Phys. Rev. Lett., 120, 241103
Lesage S. et al., 2023, ApJ, 952, L42
Li M. L. et al., 2024, preprint (arXiv:2411.07973)
Lipunov V. et al., 2022, MNRAS, 516, 4980
MacFadyen A. I., Woosley S. E., 1999, ApJ, 524, 262
Margutti R. et al., 2018, ApJ, 856, L18
Masci F. J. et al., 2019, PASP, 131, 018003
Matsumoto T., Nakar E., Piran T., 2019, MNRAS, 486, 1563
McMullin J. P., Waters B., Schiebel D., Young W., Golap K., 2007, in Shaw R. A., Hill F., Bell D. J., eds, ASP Conf. Ser. Vol. 376, Astronomical Data Analysis Software and Systems XVI. Astron. Soc. Pac., San Francisco, p. 127
Meegan C. et al., 2009, ApJ, 702, 791
Melandri A. et al., 2019a, MNRAS, 490, 5366
Melandri A. et al., 2019b, A&A, 621, A81
Mészáros P., 2006, Rep. Prog. Phys., 69, 2259
Mészáros P., Rees M. J., Wijers R. A. M. J., 1998, ApJ, 499, 301
Nakar E., Piran T., 2003, New A, 8, 141
Nakar E., Piran T., 2017, ApJ, 834, 28
Navaneeth P. K., Waratkar G., Vibhute A., Bhalerao V., Bhattacharya D., Rao A. R., Vadawale S., AstroSat CZTI Collaboration, 2023, GRB Coordinates Netw., 34725
Nayana A. J. et al., 2017, MNRAS, 467, 155
Nysewander M., Fruchter A. S., Pe'er A., 2009, ApJ, 701, 824
O'Connor B. et al., 2023, Sci. Adv., 9, eadi1405
O'Connor B., Beniamini P., Gill R., 2024, MNRAS, 533, 1629
Paczyński B., 1998, ApJ, 494, L45
Panaitescu A., Kumar P., 2000, ApJ, 543, 66
Panaitescu A., Kumar P., 2001, ApJ, 560, L49
Patterson M. T. et al., 2019, PASP, 131, 018001
Perley R. A., Chandler C. J., Butler B. J., Wrobel J. M., 2011, ApJ, 739, L1
Perley D. A. et al., 2014, ApJ, 781, 37
Perley D. A. et al., 2025, MNRAS, 537, 2362
Perrott Y. C. et al., 2013, MNRAS, 429, 3330
Pihlström Y. M., Taylor G. B., Granot J., Doeleman S., 2007, ApJ, 664, 411
Planck Collaboration VI, 2020, A&A, 641, A6
Rhoads J. E., 1997, ApJ, 487, L1
Rhodes L., van der Horst A. J., Fender R., Aguilera-Dena D. R., Bright J. S., Vergani S., Williams D. R. A., 2022, MNRAS, 513, 1895
Rhodes L. et al., 2024, MNRAS, 533, 4435
Rigault M. et al., 2019, A&A, 627, A115
Roberts O. J., Bala S., Meegan C., GBM Fermi, 2023, GRB Coordinates Netw., 34748
Rossi E. M., Perna R., Daigne F., 2008, MNRAS, 390, 675
Rossi A. et al., 2022, ApJ, 932, 1
Ryan G., van Eerten H., Piro L., Troja E., 2020, ApJ, 896, 166
Ryan G., van Eerten H., Troja E., Piro L., O'Connor B., Ricci R., 2024, ApJ, 975, 131
Salafia O. S., Ghisellini G., Pescalli A., Ghirlanda G., Nappo F., 2015, MNRAS, 450, 3549
Saraogi D. et al., 2024, MNRAS, 530, 1386
Sari R., Piran T., Narayan R., 1998, ApJ, 497, L17
Sari R., Piran T., Halpern J. P., 1999, ApJ, 519, L17

Sarin N., Ashton G., Lasky P. D., Ackley K., Mong Y.-L., Galloway D. K., 2021, preprint (arXiv:2105.10108)
Sarin N., Hamburg R., Burns E., Ashton G., Lasky P. D., Lamb G. P., 2022, MNRAS, 512, 1391
Sarin N. et al., 2024, MNRAS, 531, 1203
Sato Y., Obayashi K., Yamazaki R., Murase K., Ohira Y., 2021, MNRAS, 504, 5647
Sato Y., Murase K., Ohira Y., Yamazaki R., 2023, MNRAS, 522, L56
Schady P. et al., 2012, A&A, 537, A15
Schlafly E. F., Finkbeiner D. P., 2011, ApJ, 737, 103
Schulze S. et al., 2011, A&A, 526, A23
Sharma Y. et al., 2021, JA&A, 42, 73
Speagle J. S., 2020, MNRAS, 493, 3132
Srinivasaragavan G. P. et al., 2023, ApJ, 949, L39
Srinivasaragavan G. P. et al., 2024, ApJ, 960, L18
Srivastav S. et al., 2025, ApJL, 978, L21
Stalder B. et al., 2017, ApJ, 850, 149
Sun H. et al., 2024, preprint (arXiv:2410.02315)
Taylor G. B., Frail D. A., Berger E., Kulkarni S. R., 2004, ApJ, 609, L1
Taylor G. B., Momjian E., Pihlström Y., Ghosh T., Salter C., 2005, ApJ, 622, 986
Troja E. et al., 2018, MNRAS, 478, L18
Troja E. et al., 2019, MNRAS, 489, 1919
Tsvetkova A. et al., 2021, ApJ, 908, 83
van Dalen J. N. D. et al., 2024, preprint (arXiv:2409.19056)
van der Horst A. J. et al., 2014, MNRAS, 444, 3151
van der Walt S., Crellin-Quick A., Bloom J., 2019, J. Open Source Softw., 4, 1247
van Dokkum P. G., 2001, PASP, 113, 1420
van Paradijs J., Kouveliotou C., Wijers R. A. M. J., 2000, ARA&A, 38, 379
Vail J. L., Li M. L., Wise J., Perley D. A., Ho A. Y. Q., Burns E., Coughlin M., 2023, GRB Coordinates Netw., 34730
Walker M. A., 1998, MNRAS, 294, 307
Walker M. A., 2001, MNRAS, 321, 176
Wang X.-G. et al., 2015, ApJS, 219, 9
Wei J. et al., 2016, preprint (arXiv:1610.06892)
Xie X., MacFadyen A., 2019, ApJ, 880, 135
Xu F., Huang Y.-F., Geng J.-J., 2023, A&A, 679, A103
Ye X.-M., Wei D.-M., Zhu Y.-M., Jin Z.-P., 2024, Res. Astron. Astrophys., 24, 045011
Yuan W., Zhang C., Chen Y., Ling Z., 2022, in Bambi C., Sangangelo A., eds, Handbook of X-ray and Gamma-ray Astrophysics. Springer Nature, Cham, p. 86
Zackay B., Ofek E. O., Gal-Yam A., 2016, ApJ, 830, 27
Zwart J. T. L. et al., 2008, MNRAS, 391, 1545

SUPPORTING INFORMATION

Supplementary data are available at *MNRAS* online.

AT2023sva_spectrumflux.txt
AT2023sva_spectrumflux_errors.txt

Please note: Oxford University Press is not responsible for the content or functionality of any supporting materials supplied by the authors. Any queries (other than missing material) should be directed to the corresponding author for the article.

APPENDIX A: CORNER PLOTS

Here, we show the corner plots for the modelling described in Section 9.

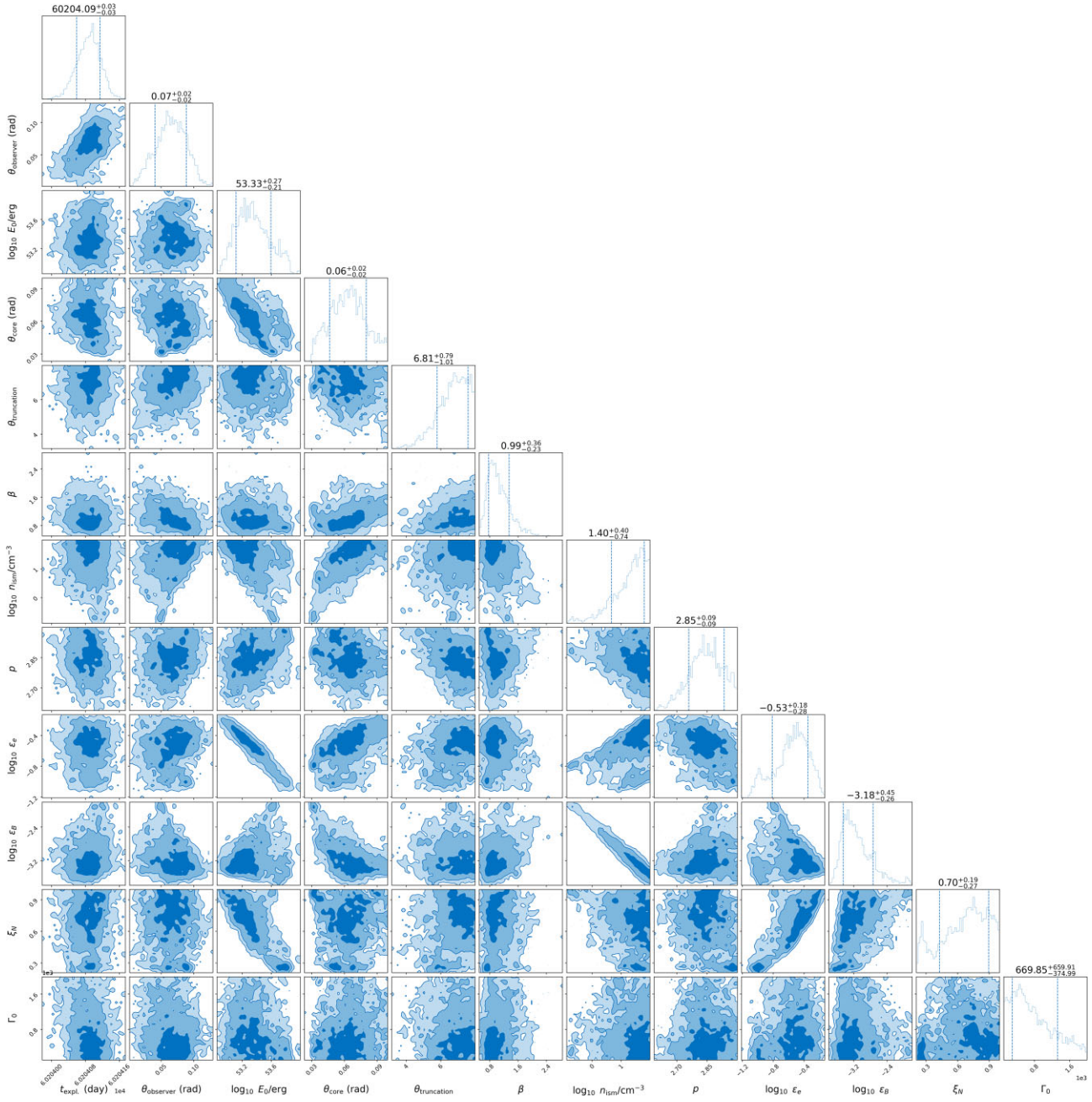

Figure A1. Corner plot for the power-law structured jet model, generated through REDBACK.

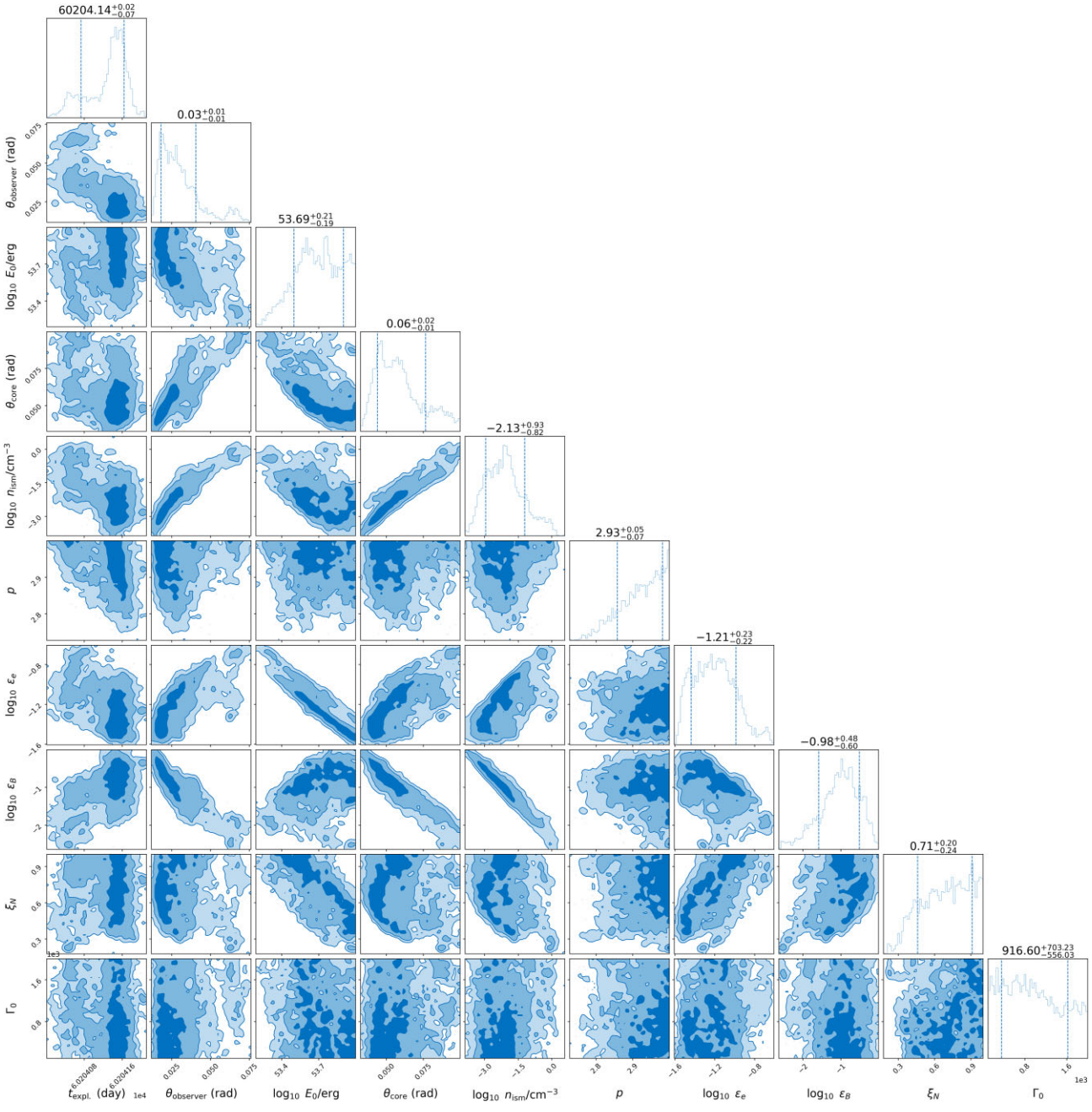

Figure A2. Corner plot for the tophat model, generated through REDBACK.

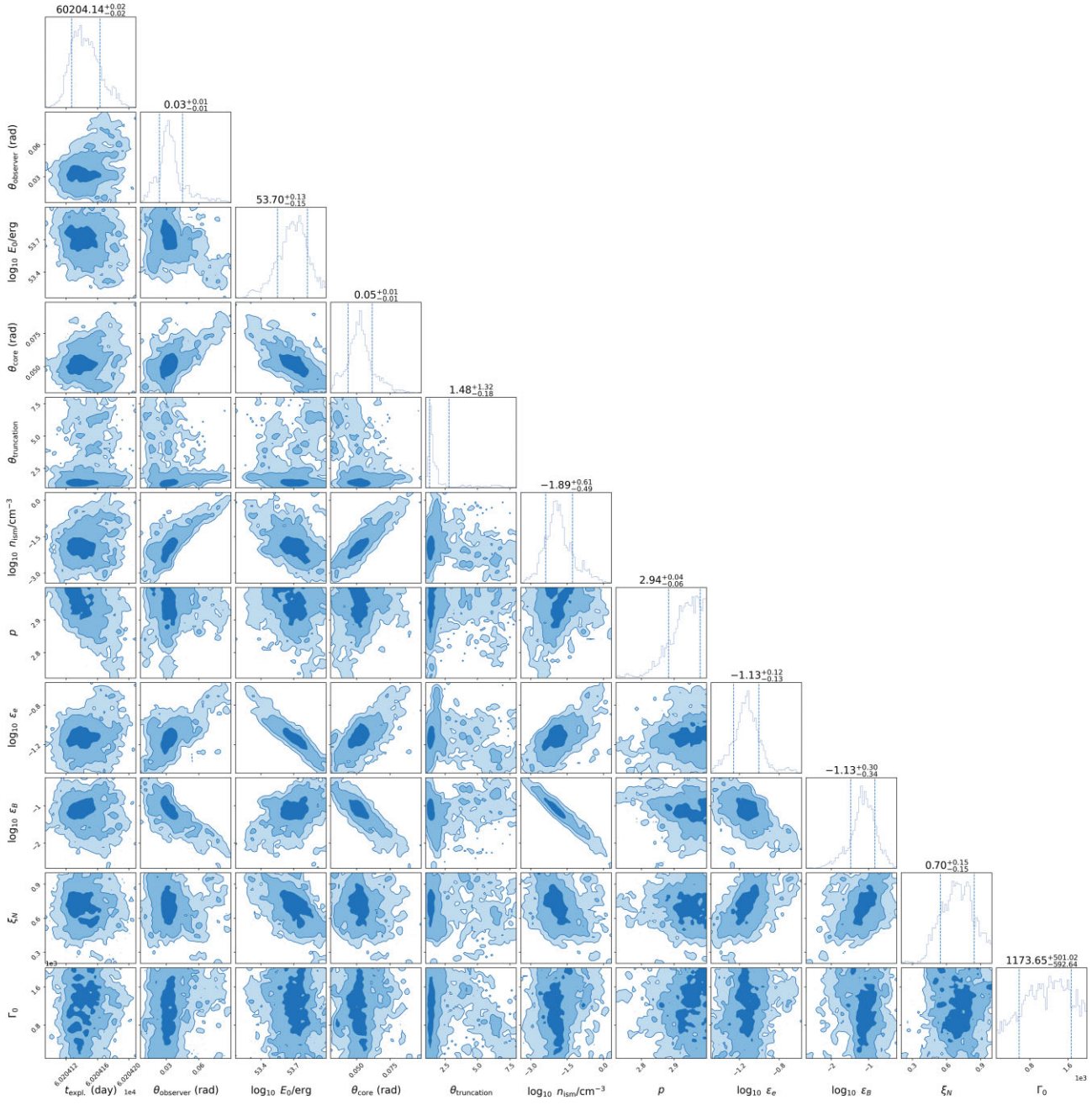

Figure A3. Corner plot for the gaussian structured jet model, generated through REDBACK.

[1]Department of Astronomy, University of Maryland, College Park, MD 20742, USA
[2]Joint Space-Science Institute, University of Maryland, College Park, MD 20742, USA
[3]Astrophysics Science Division, NASA Goddard Space Flight Center, 8800 Greenbelt Rd, Greenbelt, MD 20771, USA
[4]Astrophysics Research Institute, Liverpool John Moores University, 146 Brownlow Hill, Liverpool L3 5RF, UK
[5]Department of Astronomy, Cornell University, Ithaca, NY 14853, USA
[6]McWilliams Center for Cosmology and Astrophysics, Department of Physics, Carnegie Mellon University, Pittsburgh, PA 15213, USA
[7]Observatoire de la Côte d'Azur, CNRS, Université de la Côte d'Azur, Artemis, Nice F-06304, France
[8]LAM, CNRS, Aix Marseille Univ., Marseille 13388, France
[9]Oskar Klein Centre for Cosmoparticle Physics, Department of Physics, Stockholm University, AlbaNova, Stockholm SE-106 91, Sweden
[10]Nordita, Stockholm University and KTH Royal Institute of Technology, Hannes Alfvens vag 12, SE-106 91 Stockholm, Sweden
[11]Oskar Klein Centre, Department of Astronomy, Stockholm University, AlbaNova, SE-10691 Stockholm, Sweden
[12]Trottier Space Institute at McGill, 3550 Rue University, Montreal, Quebec H3A 2A7, Canada
[13]Department of Physics, McGill University, 3600 Rue University, Montreal, Quebec H3A 2T8, Canada
[14]Astrophysics Group, Cavendish Laboratory, 19 J J Thomson Avenue, Cambridge CB3 0HE, UK
[15]Ioffe Institute, Polytekhnicheskaya, 26, St. Petersburg 194021, Russia
[16]Department of Physics, IIT Bombay, Powai, Mumbai 400076, India
[17]National Centre for Radio Astrophysics, Tata Institute of Fundamental Research, Pune University Campus, Ganeshkhind, Pune 411007, India
[18]National Radio Astronomy Observatory, 520 Edgemont Rd, Charlottesville VA 22903, USA
[19]Cosmic Dawn Center (DAWN), Rådmandsgade 64, 2200 København N, Denmark
[20]Niels Bohr Institute, University of Copenhagen, Jagtvej 128, Copenhagen DK-2200, Denmark
[21]Department of Astrophysics/IMAPP, Radboud University Nijmegen, PO Box 9010, Nijmegen, NL-6500 GL, the Netherlands
[22]Perimeter Institute for Theoretical Physics, Waterloo, Ontario N2L 2Y5, Canada
[23]Department of Computer Science and Engineering, IIT Bombay, Powai, Mumbai 400076, India
[24]DIRAC Institute, Department of Astronomy, University of Washington, 3910 15th Avenue NE, Seattle, WA 98195, USA
[25]Department of Physics and Astronomy, Louisiana State University, Baton Rouge, LA 70803, USA
[26]Department of Physics and Astronomy, University of Turku, Vesilinnantie 5, FI-20014, Finland
[27]Caltech Optical Observatories, California Institute of Technology, Pasadena, CA 91125, USA
[28]Division of Physics, Mathematics, and Astronomy, California Institute of Technology, Pasadena, CA 91125, USA
[29]Indian Institute of Astrophysics, 2nd Block 100 Feet Rd, Koramangala, Bangalore 560034, India
[30]School of Physics and Astronomy, University of Minnesota, Minneapolis, MN 55455, USA
[31]Astrophysics, Department of Physics, University of Oxford, Keble Road, Oxford OX1 3RH, UK
[32]Centro Astronómico Hispano en Andalucía, Observatorio de Calar Alto, Sierra de los Filabres, Gérgal, Almería 04550, Spain
[33]GRANTECAN, Cuesta de San José s/n, E-38712 Breña Baja, La Palma, Spain
[34]Instituto de Astrofísica de Canarias, Vía Láctea, E-38205 La Laguna, Tenerife, Spain
[35]Center for Astrophysics, Harvard & Smithsonian, 60 Garden St, Cambridge MA 02138, USA
[36]IPAC, California Institute of Technology, 1200 E. California Blvd, Pasadena, CA 91125, USA
[37]National Radio Astronomy Observatory, PO Box 'O', Socorro, NM 87801, USA
[38]Department of Physics, Drexel University, Philadelphia, PA 19104, USA
[39]Astronomical Institute, Czech Academy of Sciences, Fričova 298, Ondřejov 251 65, Czech Republic
[40]Dipartimento di Fisica, Università degli Studi di Cagliari, SP Monserrato-Sestu, km 0.7, I-09042 Monserrato, Italy

This paper has been typeset from a TEX/LATEX file prepared by the author.